Influence of fault roughness on surface displacement: From numerical simulations to coseismic slip distributions

Lucile Bruhat[1*], Yann Klinger[1], Amaury Vallage[1,2] and Eric M. Dunham[3]

[1]*Institut de Physique du Globe de Paris, Université de Paris, CNRS UMR 7154, Paris, France*

[2]*CEA, DAM, DIF, F-91297 Arpajon, France*

[3]*Department of Geophysics and Institute for Computational and Mathematical Engineering, Stanford University, Stanford, California, USA*

[*]*Now at Laboratoire de Géologie, École Normale Supérieure, PSL Research University, Paris, France*

SUMMARY

Field studies have characterized natural faults as rough, nonplanar surfaces at all scales. Fault roughness induces local stress perturbations during slip, which dramatically affect rupture behavior, resulting in slip heterogeneity. However, the relation between fault roughness and slip heterogeneity remains a key knowledge gap between current numerical and field studies. In this study, we analyze numerical simulations of earthquake rupture to determine how roughness influences final slip. Using a rupture catalog containing thousands of dynamic rupture simulations on band-limited self-similar fractal fault profiles with varying roughness and background shear stress levels, we quantify how fault roughness affects the spectral characteristics of the resulting slip distribution. We find that slip distributions become increasingly more self-affine, that is, containing more short wavelength fluctuations as compared to the self-similar fault profiles, as roughness increases. We also find that, at very short wavelengths ($<$1km), the fractal dimension of the slip distributions dramatically changes with increasing roughness, background shear stress,

and rupture speed (sub-Rayleigh vs. supershear). The existence of a critical wavelength around 1 km, under which more short wavelengths are either preserved or created, suggests the role of rupture process and dynamic effects, together with fault geometry, in controlling the final slip distributions. The same spectral analysis is performed on high-resolution coseismic surface slip distributions from a catalog of real strike-slip earthquakes. Compared to numerical simulations, all earthquakes feature slip distributions that are much more self-affine than the slip distributions from numerical simulations. A different critical wavelength, here around 5-6 km, appears, potentially informing about a critical asperity length. While we show here that the relation between fault roughness and slip is much more complex than expected, this study is a first attempt at using statistical analyses of numerical simulations on rough faults to investigate observed coseismic slip distributions.

Key words: Earthquake dynamics, Rheology and friction of fault zones, Dynamics and mechanics of faulting, Mechanics, theory, and modelling.

1 INTRODUCTION

While the simplest description of a fault assumes a planar surface, it has been widely recognized that natural fault surfaces are fractal, with deviations from planarity at all scales (Power & Tullis 1991, 1995; Candela et al. 2009, 2012). This characteristic, often described as fault roughness, has considerable influence on earthquake rupture behavior. On a rough fault, both shear and normal local stresses are perturbed during fault slip, leading to complex rupture behavior. Manifestations of this complexity include rapid accelerations and decelerations of the rupture front, slip heterogeneity (Chester & Chester 2000; Dieterich & Smith 2009; Dunham et al. 2011b; Shi & Day 2013), resistance to slip (Dieterich & Smith 2009; Fang & Dunham 2013), supershear transitions (Bruhat et al. 2016), variability in moment release (Zielke et al. 2017), in nucleation processes (Harbord et al. 2017; Tal & Hager 2018; Tal et al. 2018; Ozawa et al. 2019), and inelastic deformation (Hirakawa & Ma 2018). Such rupture behavior is also of particular interest to earthquake engineers when modeling building response, since rupture variability produces high frequency waves, and subsequent ground motion (Haskell 1964; Spudich & Frazer 1984; Dunham et al. 2011b; Shi & Day 2013). Irregularities in fault geometry provide a simple explanation for commonly observed spatial and temporal variations of fault slip (Andrews 1980). However, further studies of the influence of fault roughness on earthquake source parameters are still needed to unravel the physical mechanisms relating fault geometry to rupture behavior.

This study explores how fault roughness affects the slip distribution produced during an earthquake. Through a statistical analysis of a thousand dynamic rupture simulations on nonplanar fault profiles compiled in Fang & Dunham (2013) and Bruhat et al. (2016), we demonstrate that the fractal dimension of slip evolves with fault roughness, background shear stress, and rupture velocity. We document the spectral characteristics of the final slip distribution, especially at very short wavelengths. We then perform the same spectral analyses on high-resolution coseismic surface slip distributions from real strike-slip earthquakes and compare them with numerical results. Through this work, we attempt to quantify the relationship between fault roughness and observed slip distributions.

While the slip distribution due to a constant stress drop on a planar fault in a uniform elastic whole-space is elliptical, with symmetry about the center of the fault (Bilby & Eshelby 1968), analytical and numerical studies have shown for decades that the slip distribution is easily affected by changes in fault strength, fault geometry, and the mechanical properties of the surrounding rock (e.g. Bürgmann et al. 1994). In nature, the slip distribution after a large earthquake can vary greatly, from close to elliptical (as in Klinger et al. 2011; Choi et al. 2018) to highly irregular (as mentioned in Scholz 2019). The shape and amplitude of the slip distribution is often interpreted a posteriori as a consequence of some known properties of the fault, such as complexities in the fault geometry or variations in rock properties. However, due to our lack of knowledge of characteristics of the fault and

surrounding medium, it remains very difficult to predict detailed slip distributions. Thanks to the large amount of measured slip distributions, statistical analyses such as Manighetti et al. (2005) have tried to quantify generic features of cumulative slip; however, given a single coseismic slip distribution, it is still challenging to determine which fault properties are responsible for its characteristics.

The relationship between fault roughness and slip also remains complex. Early on, field studies noticed differences in fault geometry with cumulative slip. Faults that have slip larger than 10–100 m appear to show lower root-mean-square (RMS) deviations from planarity than newly-created faults (Sagy et al. 2007; Sagy & Brodsky 2009). Fault wear can occur through various mechanisms, such as abrasion, grinding, grain plucking, and fault splaying. While faults appear to gradually smooth with increasing slip, recent studies have emphasized that, because wear involves both smoothing and re-roughening mechanisms, leading to a slow and inefficient process, it remains difficult to constrain the degree of smoothing with slip (Brodsky et al. 2011; Shervais & Kirkpatrick 2016). Compilations of fractal dimension of exhumed fault surfaces ranging from 50 μm to 10 m and surface ruptures from major continental strike-slip earthquakes in Candela et al. (2012) suggest that fault geometries all share the same self-affine characteristics with a Hurst exponent around 0.6 in the slip direction. Unlike previous work relating displacement to fault smoothing, they found no significant relationship between the roughness amplitude and cumulative slip. This would imply that fault maturity, the notion that faults inevitably smooth with cumulative slip, might still be an ambiguous process.

In the meantime, significant progress in imaging coseismic slip distributions has been made. Sub-pixel image correlation of combined optical and radar satellite images is now commonly used to produce maps of the 3D components of the surface displacement field due to an earthquake (Leprince et al. 2007; Rosu et al. 2015). Beyond the improved description of coseismic displacement, with a pixel size of the order of 1 to 10 meters, which leads to measurements along fault every 100-200 meters, these techniques allow the identification of near-field inelastic deformation features around geometrical complexities (Milliner et al. 2015; Vallage et al. 2015), which might be related to off-fault coseismic damage (Klinger et al. 2018). Studying such precise measurements might provide us a new way at relating the fault fractal dimension to the coseismic slip distribution. When measurements of fault roughness remain scarce and onerous, one could think that the fractal dimension of the fault would leave an imprint in the coseismic slip distribution. If such imprint exists, and is quantifiable, coseismic slip distributions would inform us about fault roughness, and by process of elimination, might help us to better identify the other mechanical processes affecting the slip distribution.

In the present work, we pursue this strategy to study how roughness influences final slip distributions. We first analyze numerical simulations of earthquake rupture in a statistical manner to document the effect of roughness on slip. For that, we consider the rupture catalog described in Fang & Dunham

(2013) and Bruhat et al. (2016), which contains several thousand rupture simulations on self-similar faults ($H = 1$) with six values of roughness α and various background shear stress levels. While most numerical studies are based on the analysis of one or a few individual ruptures, Fang & Dunham (2013) built an ensemble of 2-D plane strain dynamic simulations on rough faults in order to allow a statistical characterization of the rupture behavior. They focused their analysis on evaluating the roughness drag, the additional shear resistance to slip due to fault roughness. Following that, Bruhat et al. (2016) documented rupture style on rough faults for both sub-Rayleigh and supershear ruptures. They showed that even though supershear transients are more likely on rougher faults, sustained supershear rupture tends to occur on smoother fault segments.

In this study, we return to this ensemble database and perform various spectral analyses to document statistically how final slip profiles evolve with increasing roughness and background shear stress. We find that for ruptures on self-similar faults ($H = 1$), increasing roughness leads to slip profiles deviating from self-similarity, with Hurst coefficients down to 0.6. We also show that at very short wavelengths ($\leq$1 km), the slope of the power spectral density dramatically changes with roughness, background shear stress, and rupture speed (sub-Rayleigh vs. supershear). Finally, we perform the same spectral analyses on high-resolution coseismic slip distributions from real earthquakes, and compare them to our numerical results. This work constitutes a first attempt at connecting numerical simulations of rough faults to observed coseismic slip distributions.

2 DYNAMIC RUPTURE SIMULATIONS ON SELF-SIMILAR ROUGH FAULTS

We review here the numerical methods developed by Dunham et al. (2011a,b) and Fang & Dunham (2013) to build a collection of 2D plane strain dynamic rupture simulations on nonplanar fault profiles.

Fault roughness is commonly quantified as follows. Consider a 1D fault profile $y = h(x)$ with zero mean. This fault is defined as fractal when the power spectral density of $h(x)$ is of the form

$$P_h(k) \sim |k|^{-\beta}, \tag{1}$$

where β ranges from 1 to 3. Both the fractal dimension D and the Hurst coefficient H relate to this exponent, such that for a 1D profile $D = (5 - \beta)/2$ and $H = (\beta - 1)/2$ (Turcotte & Huang 1995). For a self-similar fractal, $\beta = 3$, $D = 1$, and $H = 1$. Such a profile has root-mean-square (RMS) deviations from planarity h_{RMS} proportional to the fault length L:

$$h_{\text{RMS}} = \alpha L. \tag{2}$$

where α is the amplitude-to-wavelength ratio of roughness. Field studies show that α varies, in the slip-parallel direction, between 10^{-3} to 10^{-2} (Power & Tullis 1991). Depending on the study, fault rough-

ness either designates the fractal dimension D, and its associated Hurst coefficient, the amplitude-to-wavelength ratio α, or all of them. In this study, as we mostly consider self-similar fault profiles, the term "roughness" designates the amplitude-to-wavelength ratio α. Any difference in Hurst coefficient will be clearly labeled as such.

Recent high-resolution measurements of surface roughness at scales below 100 m suggested that natural faults are not self-similar, but self-affine (Renard et al. 2006; Candela et al. 2009, 2012). Self-affine fractals have Hurst exponents below 1 (corresponding to $\beta < 3$ in equation 1). While self-similar fractals have statistically similar appearance independent of the observation scale, self-affine profiles appear smoother at larger scales. However, as discussed by Dunham et al. (2011b), no single power law spectral density has been found yet to fit both the outcrop and the map scale. Shi & Day (2013) also showed that self-similar models have the potential to make this connection across observation scales. Likewise, over the several orders of magnitude in scale that can be currently simulated, differences between self-similar and self-affine characteristics are expected to be small. The use of a self-similar model, prominent in recent numerical studies (Fang & Dunham 2013; Bruhat et al. 2016; Zielke et al. 2017; Hirakawa & Ma 2018), is therefore the logical starting point to begin quantifying the effect of fault roughness on slip.

This study makes use of 100 randomly-generated faults profiles for six values of α ranging from 0.001 to 0.012. The fault profiles are all self-similar ($H = 1$). The ensemble presented in Fang & Dunham (2013) and Bruhat et al. (2016) considered roughness up to $\alpha = 0.01$, not 0.012. In this study, we added additional simulations for $\alpha = 0.012$ and new values of background shear stress. Rough faults are described by a 1D profile $y = h(x)$, shown in Figure 1, embedded in an homogeneous medium, infinite in extent. The profile length is 60 km and the grid spacing is Δx = 10 m. We set the initial stress field σ_{ij}^0 to be spatially uniform, described by the background shear stress $\tau_0 = \sigma_{xy}^0$, the effective normal stress $\sigma_0 = -\sigma_{yy}^0$, and the angle Ψ between the maximum principal compressive stress and the x-axis. For all simulations, $\sigma_0 = 126$ MPa and $\Psi = 50°$.

We use a rate-and-state friction law, evolving toward a strongly velocity-weakening steady state strength to perform the dynamic simulations. This friction law allows the propagation of a self-healing slip pulse at low background shear stress τ_0 (Zheng & Rice 1998; Dunham et al. 2011b). The background shear stress ranges from 35.0 MPa (τ_0/σ_0 = 0.28) to 56 MPa (τ_0/σ_0 = 0.44). As shown by Fang & Dunham (2013), the minimum τ_0 at which self-sustaining propagation is possible increases with the roughness α. A nonplanar geometry will induce stress concentrations at geometric complexities To limit these stresses and prevent fault opening, the off-fault material is characterized by a noncohesive elasto-viscoplastic rheology. We will explore the potential effect of the details of the elasto-viscoplastic rheology later in the study. Rupture is artificially initiated at the point of highest

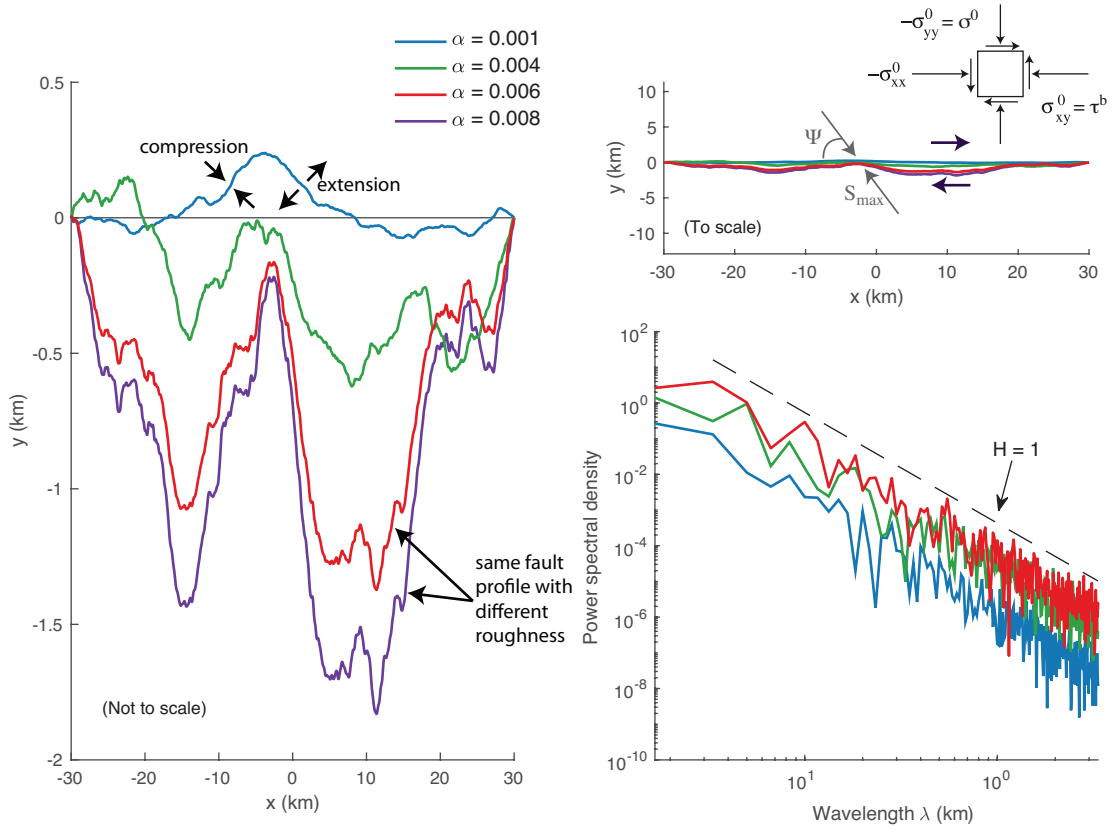

Figure 1. Left: Examples of three band-limited self-similar faults, for four roughness values ($\alpha = 0.001$, 0.004, 0.006, and 0.008), exaggerated in the y-direction, illustrating compressional and extensional bends. Top right: Plane strain model with right-lateral slip on the same faults to scale. The medium is loaded with a spatially uniform stress state, with the maximum principal stress inclined at an angle $\Psi = 50°$ to the fault. Bottom right: Corresponding power spectral density. They all follow a power spectra law of the form $|k|^{-\beta}$ where k the wavenumber and $\beta = 3$ (or $H = 1$), which defines the profiles as self-similar.

resolved shear-to-normal stress ratio by applying a localized shear stress perturbation. Each simulation generates an individual rupture, initially propagating bilaterally. Secondary ruptures of the fault sometimes occur (examples of such complexity were analyzed in Bruhat et al. (2016)). However, there is no possibility here for any fault segmentation or branching. Finally, no earthquake sequence modeling is included here, which means that the simulation stops once the rupture fully arrests. Further details on the modeling approach for rough faults can be found in Dunham et al. (2011a,b), and Fang & Dunham (2013). The numerical methods are described in Dunham et al. (2011a) and Kozdon et al. (2012, 2013).

Our work focuses on a catalog of 2D plane strain dynamic rupture simulations to analyze the rupture behavior in a statistical manner. As we vary the fault profile, the rupture will behave differently for each simulation. However, by considering a large amount of fault traces, and their associated

ruptures together, we are able to discriminate properties of the rupture behavior that are independent of the original fault profile. We do recognize that the recent development of 3D dynamic earthquake rupture simulations (Shi & Day 2013; Duru & Dunham 2016; Yao 2017; Ulrich et al. 2019) might change some of our results from 2D simulations. However, because 3D simulations remain computationally challenging, the statistical approach that we propose here has not been applied to 3D rupture simulations yet.

3 INSIGHTS FROM NUMERICAL SIMULATIONS

In this section, we document the influence of fault roughness on the characteristics of the slip distribution obtained from the rupture catalog described in the previous section. For each numerical simulation, we consider the final slip distribution. We limit our analysis to well-developed ruptures, defined by having a final length larger than 10 km. The reasons behind this choice are first to avoid transient ruptures, and also to be able to compare the results from this numerical catalog to high-resolution data real earthquakes ruptures, which are, for now, mainly produced for well-developed long ruptures. To avoid nucleation effects, we also exclude the region near the hypocenter in the following analysis.

3.1 Effect on fractal character of the slip distribution

As described in section 2, the fault traces in the rupture catalog are all self-similar ($H = 1$). For each rupture realization, we compute the power spectral density of the final slip distribution. We restrict our analysis to wavelengths exceeding the minimum roughness wavelength λ_{min}= 0.3 km. Due to the finite size of the domain used for the Fourier transform and the fact that most ruptures cover a substantial part of the domain, the maximum wavelength relates here to the domain size in the along-strike direction (60 km). Examples of final slip and corresponding power spectral density are displayed in Figure 2. Like the fault profiles, the slip distributions are fractal with power spectral density described by a power law $|k|^{-\beta}$ at high wavenumber, i.e., small wavelength. At wavelengths higher than the rupture length, the spectrum becomes flat.

Using the power spectral densities of each slip distribution, we obtain the mean power spectral density of slip for a set of roughness α and background shear stress τ_b. We then derive the slope of the power spectral density β, and the corresponding Hurst coefficient using the relation $H = (\beta - 1)/2$. Because we consider only slip distributions having lengths larger than 10 km, the slope of power spectral density is computed between 10 km and the minimum roughness wavelength λ_{min} = 0.3 km.

The evolution of the mean Hurst coefficient of the slip profiles for ruptures with varying fault roughness and background shear stress is displayed in Figure 3. At low roughness ($\alpha = 0.001$) Hurst

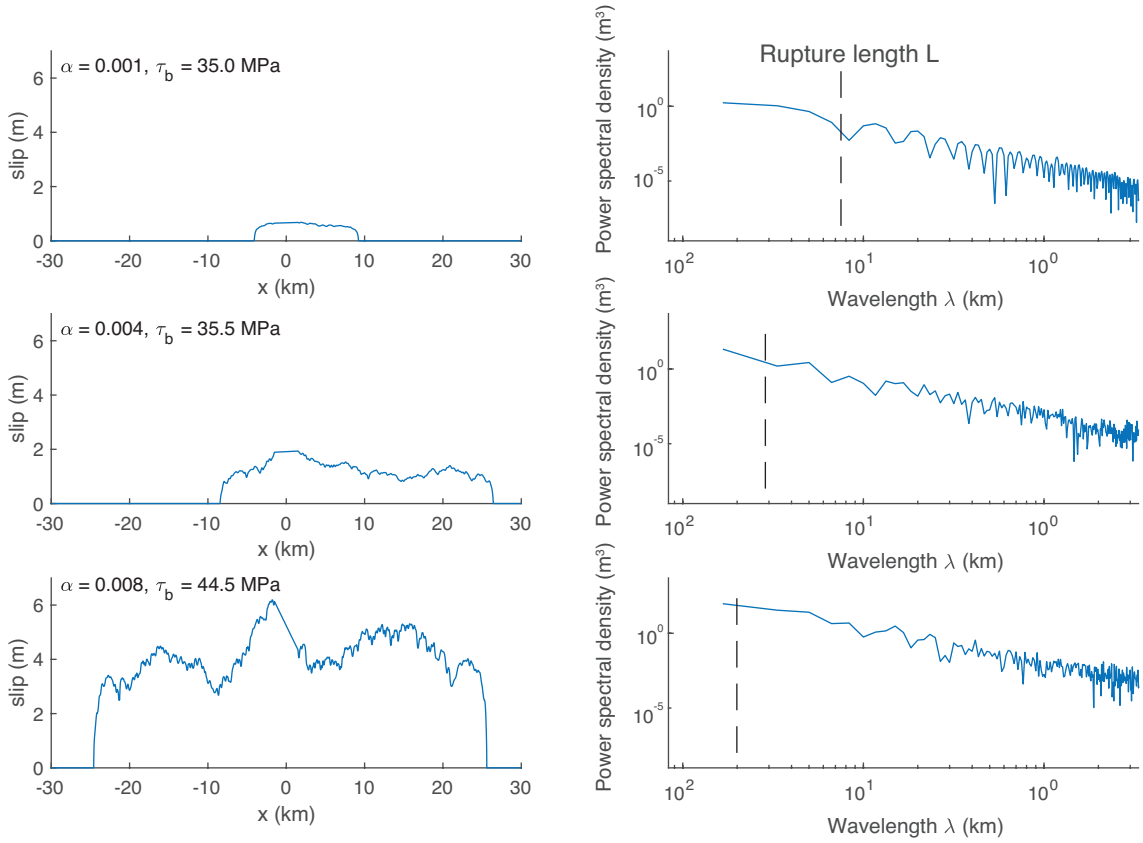

Figure 2. Final slip distributions (left panel) for three roughness values ($\alpha = 0.001, 0.004$ and 0.008). Corresponding power spectral densities are displayed in the right panel. At wavelengths smaller than the rupture length L, on the right side of the figure, the spectrum is described by a power law $|k|^{-\beta}$, where k the wavenumber. At wavelengths larger than L, the spectrum becomes flat. The flat part of the spectrum is more visible for the rupture in the top panel, as its length is much smaller than the domain size.

coefficients are close to 1. So for a very smooth fault, the slip distribution is also a self-similar fractal distribution. As the roughness increases, the Hurst coefficients decrease, down to 0.6 for the roughest faults ($\alpha = 0.012$). In other words, increasing roughness, up to $\alpha = 0.006$, leads to slip distributions increasingly deviating from self-similarity. Above $\alpha = 0.006$, the distribution of mean Hurst coefficients seems to saturates around $0.55 - 0.7$. Note that this trend appears to be weakly influenced by background shear stress.

As shown in Bruhat et al. (2016), for the considered values of background shear stress, supershear transients are more likely to occur when fault roughness exceeds $\alpha = 0.006$. Figure 4 displays the evolution of Hurst coefficients when distinguishing sub-Rayleigh from supershear ruptures. As explained earlier, only ruptures that show the same behavior (sub-Rayleigh vs. supershear) over at least 10 km are considered. Figure 4 shows that only sub-Rayleigh ruptures exhibit the inverse relationship between roughness and Hurst coefficient. On the other hand, slip distributions from supershear rup-

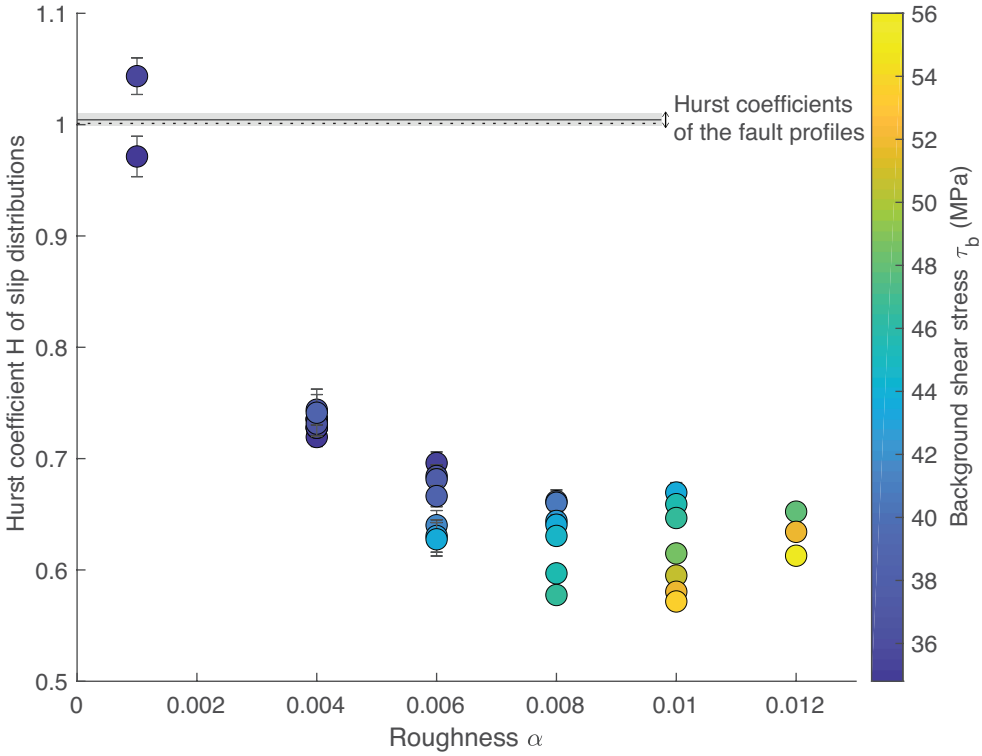

Figure 3. Evolution of the mean Hurst coefficient of final slip profiles for ruptures with varying fault roughness (x-axis) and background shear stress (colored scale). Error bars correspond to 1-σ uncertainties. The range of Hurst coefficients of the original fault traces is also displayed. Note that, although the fault profiles were generated such that $H = 1$, the uncertainty comes from the fault generation and the fitting methods. Very smooth faults ($\alpha = 0.001$) present Hurst coefficients of slip around 1, meaning that the slip profile is self-similar. Increasing roughness leads to lower Hurst coefficients, down to ~ 0.6. Values of $H < 1$ indicate that the slip distribution are not self-similar, but self-affine.

tures all display Hurst coefficients ranging from 0.55 to 0.7. Figures 3 and 4 show that fault roughness promotes slip distributions that are more self-affine than the original fault profiles. Although the fractal character of the resulting slip distribution is relatively independent of background shear stress, it is affected by rupture velocity and fault roughness.

3.2 Focus on the shorter wavelengths

In the previous section, we estimated the slope of the power spectral density, which is computed between the minimum wavelength and 10 km. This section first focuses on examining characteristics of the power spectral densities as a function of wavelength. Figure 5 displays the mean power spectral density of the final slip distributions, for all considered α and τ_b, as a function of the wavelength λ. As mentioned earlier in this study, resulting spectra all decay at shorter wavelengths. We still notice

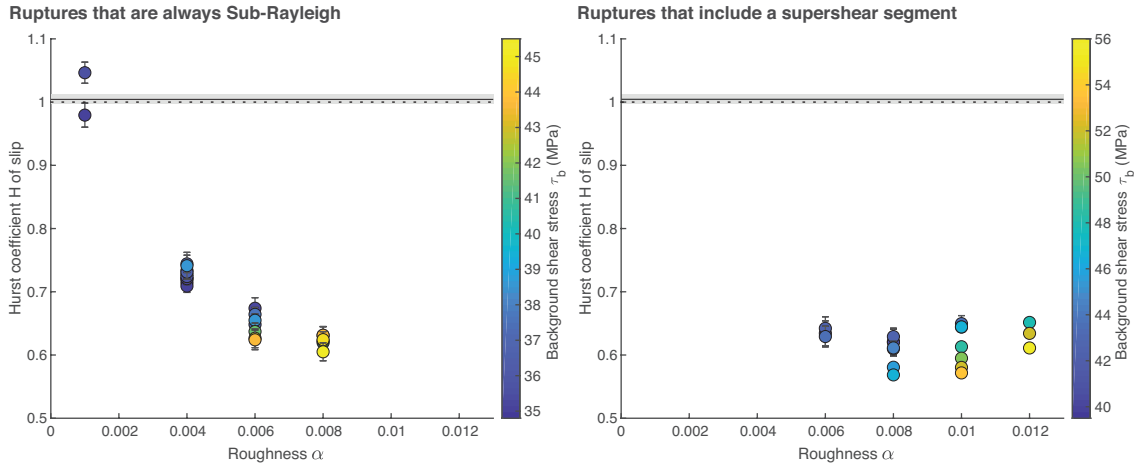

Figure 4. Distribution of Hurst coefficients when distinguishing between sub-Rayleigh and supershear ruptures. As roughness increases, the slip distribution of sub-Rayleigh ruptures deviate from self-similarity. Supershear ruptures, occurring mostly on very rough faults, all show slip profiles that are self-affine, with $H \sim 0.6$.

differences between the level of roughness and background shear stress. First, the slope at short wavelengths increases with both α and τ_b. The difference is striking between the slope observed in the spectra for $\alpha = 0.001$ as compared to $\alpha = 0.008$. Increasing roughness leads to a greater content in short wavelengths in the final slip distributions. However, this change appears to be wavelength-dependent. When focusing on the spectra for $\alpha = 0.004$, we notice that 1.) the slope at very short wavelengths ($<$1 km) differs from the one at longer wavelengths; and that 2.) when increasing the background shear stress, the slope evolves dramatically at wavelengths smaller than 1 km. Note that the value at the longest wavelengths, which relates to the moment, also increases with roughness, but this increase is mostly due to increases in background shear stress, and hence stress drop.

In order to better study this behavior, we compute the power spectral density of the slip gradient distribution, instead of the slip profile. This is the slip gradient computed with respect to the average along-strike distance x. Using the gradient will help us to better distinguish changes in slope at short wavelengtsh. Figure 6 illustrates the resulting density for $\alpha = 0.004$ and $\alpha = 0.006$. We observe a sharp change in slope at $\lambda \sim 1$ km. Consider the power spectral density for $\alpha = 0.006$ and $\tau_b = 35.3$ MPa. The slope at which the density decreases appears to remain the same in the entire wavelength domain. Now, consider a spectrum at higher background shear stress; at wavelengths shorter than 1 km, the slope of the spectrum gradually increases, ultimately changing sign, suggesting larger power at shorter wavelengths. Note the difference between the spectra for $\tau_b = 35.3$ MPa and $\tau_b = 43.5$ MPa: the slopes at $\lambda < 1$ km present opposite signs. The critical wavelength, at which the change in wavelength content appears, also varies with the roughness α. For this particular example, increasing roughness leads to larger critical wavelengths. The critical wavelength appears to also de-

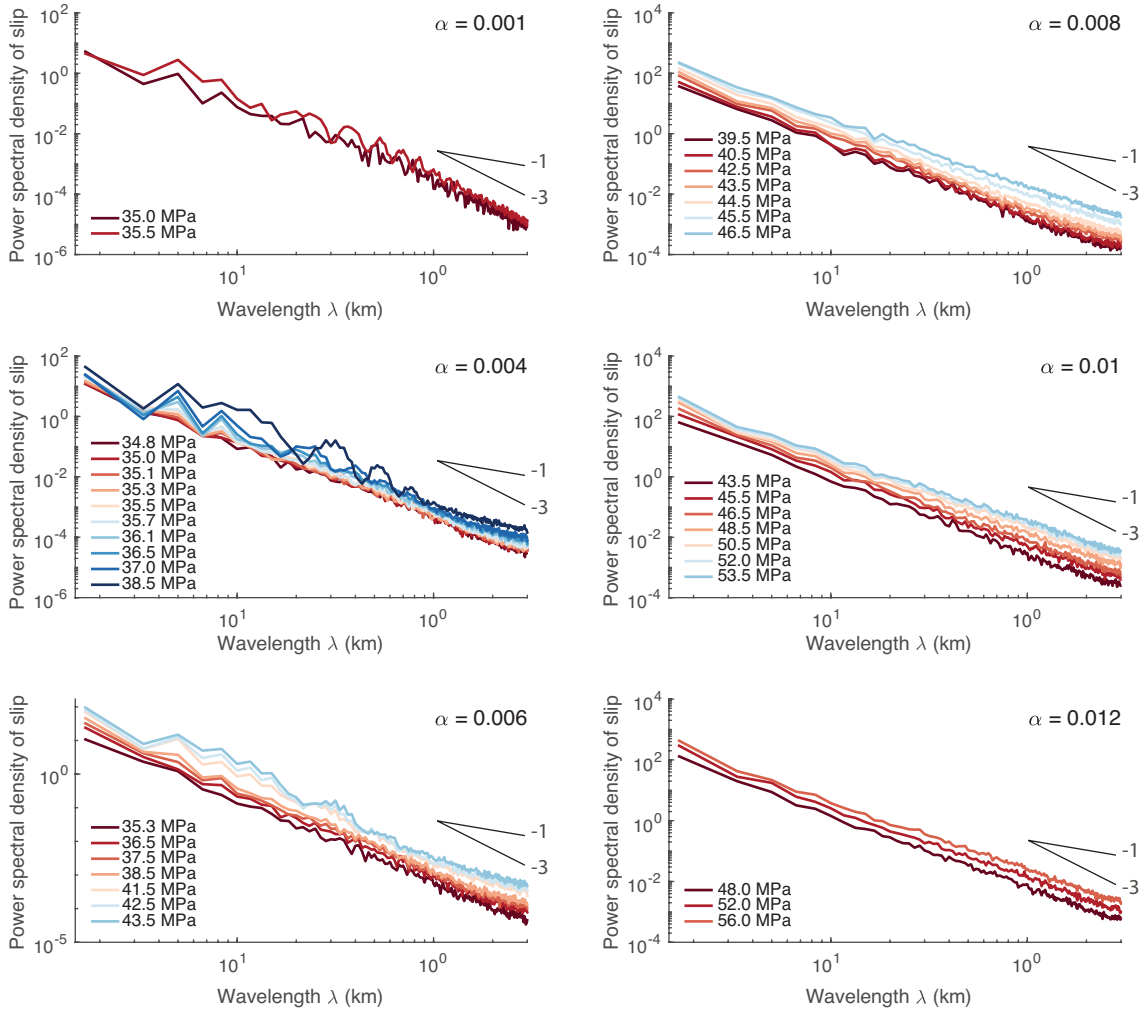

Figure 5. Mean power spectral density of final slip distributions as a function of wavelength λ and background shear stress, for roughness values from $\alpha = 0.001$ to 0.012.

pend on the background shear stress, as we notice that the sharp bend slightly moves to the left, toward longer wavelength, when increasing the background shear stress.

Following the same approach used in Figure 3, we now compare the slope of the power spectral densities of the slip distribution, by estimating the Hurst coefficient at very short wavelengths ($\lambda <$ 1 km) for all levels of roughness and background shear stress we consider in this study. Results are displayed in Figure 7. The slip distributions on the smoothest faults show Hurst coefficients close to 1, similar to the coefficients obtained in Figure 3. As the fault roughness increases up to $\alpha = 0.006$, the Hurst coefficient decreases dramatically from ~ 1 to almost 0.3. At higher roughness levels, the coefficient slightly increases up to 0.6. While the results in Figure 3 hinted at a possible dependence on background shear stress, in this case, as we focus on the very short wavelengths, the Hurst coefficient clearly decreases with increasing background shear stress for $\alpha = 0.004$ and

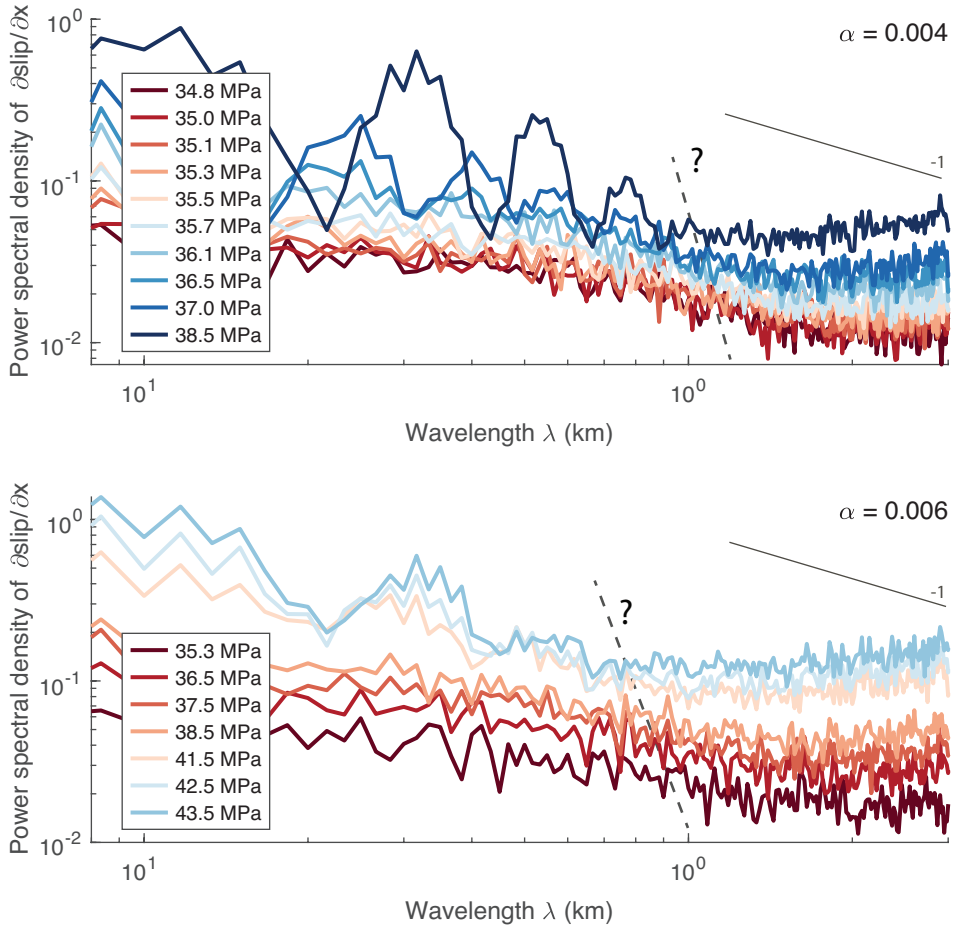

Figure 6. Mean spectra of the gradient of final slip distributions as a function of wavelength λ and background shear stress, for two roughness values.

0.006 (also see Figure A1). The relationship seems less obvious, and is possibly even reversed, for $\alpha \geq 0.006$. This might, once again, correspond to the appearance of more complex rupture behavior, such as multiple ruptures or supershear transitions (Bruhat et al. 2016).

As we notice that the change in Hurst coefficient appears around $\alpha = 0.006$, we separate ruptures that are only sub-Rayleigh from ones that include supershear segments in Figure 8. The distinction between the two trends in Hurst coefficients becomes clearer. As roughness increases, slip distributions from Sub-Rayleigh ruptures contain more shorter wavelengths. Increasing background shear stress emphasizes the slope reduction at short wavelength. In other words, as background shear stress increases, the final slip distribution will imprint more short wavelength content due to fault roughness. This might reflect that, as the background shear stress increases, the gradient of the resolved stress on the faults also rises, resulting in a higher content of short wavelengths in the final slip distribution. Note that at $\alpha = 0.008$, although still sub-Rayleigh, the rupture becomes more complex by exhibiting secondary ruptures or rupture jumps (as shown in Bruhat et al. 2016). In this case, the final slip dis-

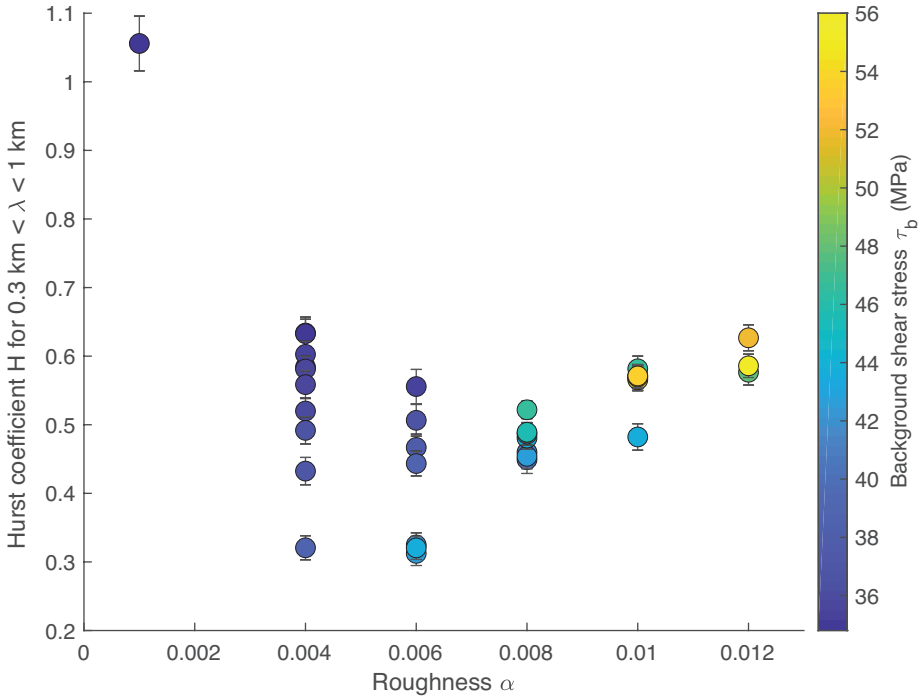

Figure 7. Evolution of the Hurst coefficient of the power spectra densities of the slip distribution, at very short wavelengths (λ <1 km). Error bars are for 1-σ uncertainties. Smooth faults display Hurst coefficients close to 1, meaning that the slip profile is self-similar. As roughness increases, the Hurst coefficients drops.

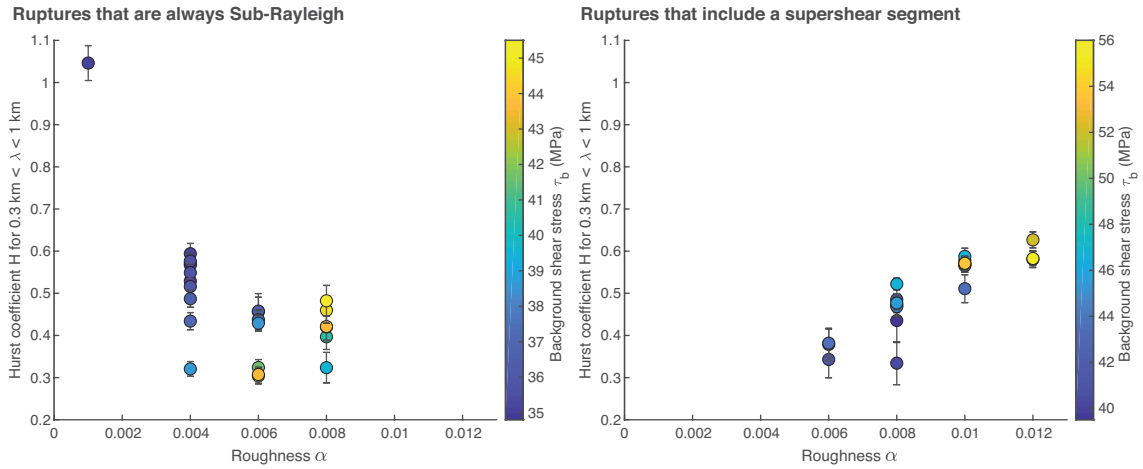

Figure 8. Distribution of the Hurst coefficient of the power spectral densities of the slip distribution at very short wavelengths (λ <1 km) when distinguishing between sub-Rayleigh and supershear ruptures. As roughness and background shear stress increase, the Hurst coefficient decreases, meaning that short wavelength fluctuations in slip for sub-Rayleigh ruptures increase. On the other hand, supershear ruptures, occurring mostly on very rough faults, all show an inverse relationship between short wavelength content and both roughness and background shear stress.

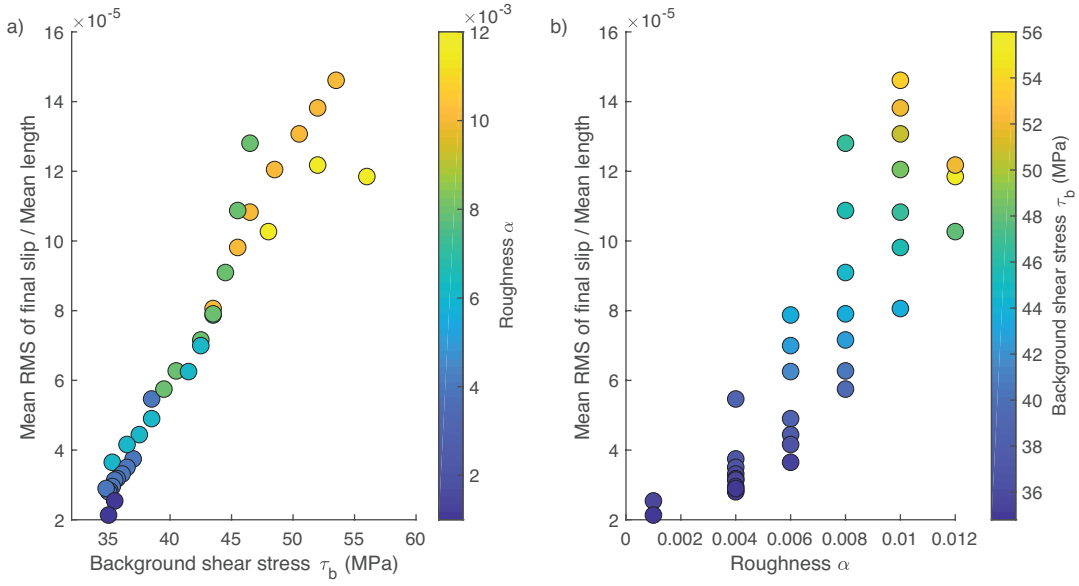

Figure 9. Distribution of root-mean-square slip for a given set of background shear stress and roughness. (Left) Linear relationship between the normalized root-mean-square slip and background shear stress, independently of the fault roughness. (Right) Normalized root-mean-square slip as a function of roughness. The fault roughness does not seem to have much of effect on root-mean-square slip that is not already captured by the need for higher stress to rupture rougher faults.

tribution renders the total slip history, which cannot be limited to simple single ruptures. Secondary ruptures of a region that had already ruptured might, for instance, smooth the final slip profiles, which could lead to less short wavelengths, or higher Hurst coefficients. This could explain the stabilization of the range of Hurst coefficients at $\alpha = 0.008$ independently of the background shear stress.

When looking at supershear ruptures, the short wavelength content in slip distributions decreases with both roughness and background shear stress. In other words, as the fault roughness or the background shear stress increases, rupture are less affected by fluctuations in fault geometry. The discrepancy with the sub-Rayleigh regime might come from differences in the process zone size evolution, as it scales differently for sub-Rayleigh and supershear ruptures (Huang & Gao 2001). However, this behavior might, once again, also result from the large rupture complexity observed at this level of roughness. As seen in Bruhat et al. (2016), multiple rupture of the same fault becomes more and more frequent leading to a final slip distribution that is not anymore representative a single rupture front, and might result in the observed discrepancy.

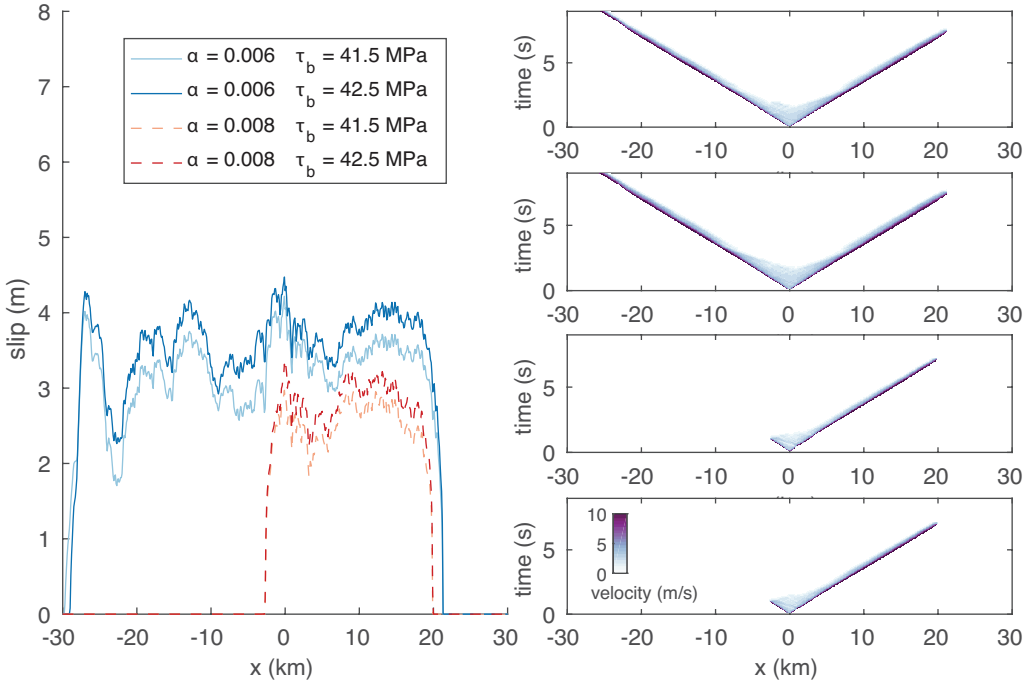

Figure 10. Influence of roughness and background shear stress on slip characteristics with $\alpha = 0.006$ and 0.008. Increasing the background shear stress increases the final slip, while additional roughness impedes rupture propagation, thereby decreasing rupture length and slip amplitude.

3.3 Effect on the amplitude of the slip distribution

We finally investigate the effect of roughness on slip amplitude, by analyzing the root-mean-square slip. The root-mean-square slip of each final slip profile of length greater than 10 km is computed, then ensemble averaged over all realizations. Figure 9 presents the distribution of root-mean-square slip for a given set of background shear stress and roughness. As the rupture length is an important factor when considering the root-mean-square slip (Dieterich & Smith 2009), we normalize the mean root-mean-square slip by the mean rupture length. The normalized root-mean-square slip of the ensemble is described twofold: as a function of the roughness and as a function of the background shear stress. Figure 9.a shows that the normalized root-mean-square slip increases linearly with the background shear stress, with only weak dependence on the fault roughness. This trend is similar to equation (8) of Dieterich & Smith (2009) that relates fault slip to length and applied stress. The normalized root-mean-square slip also increases with fault roughness α, as shown in Figure 9.b; however, this increase is mostly due to the higher background shear stress needed for self-sustaining rupture on a rougher fault.

Figure 10 illustrates these relationships for a simple bilateral sub-Rayleigh rupture. We plot the final slip profiles for two values of the background shear stress τ_b and for two levels of roughness

α. The competing effect between the background shear stress and the fault roughness is emphasized here, as the amplitude of the final slip distribution increases with the background shear stress, while increasing fault roughness promotes lower rupture length and slip amplitude. This last result is similar to conclusions by Dieterich & Smith (2009) and Fang & Dunham (2013). Both studies showed that roughness induces an additional shear resistance to slip proportional to α^2. At fixed background shear stress, as the geometrical roughness drag increases, slip decreases. In summary, Figures 9 and 10 showed that the slip amplitude relates mostly to background shear stress, and not as much to fault roughness. This relation is close to linear between the root-mean-square slip and the background shear stress.

4 COMPARISON WITH REAL STRIKE-SLIP DISTRIBUTIONS

In this section, we compare the results from our numerical simulations with coseismic displacement (i.e., slip) profiles from large strike-slip earthquakes: the 1992 M_w = 7.3 Landers, the 1999 M_w = 7.1 Hector Mine, the 2013 M_w 7.7 Balochistan, and the 2016 M_w 7.8 Kaikoura earthquakes. These events were chosen because they all occurred on well-defined strike-slip faults with high-resolution measurements of coseismic surface displacements, which would constitute an appropriate analog to our 2D plane strain dynamic rupture simulations. For each coseismic slip profile, we follow the same analysis done with the numerical simulations by computing the power spectral density to determine Hurst coefficients and investigate its behavior at short wavelengths.

We take advantage of published maps of horizontal displacements due to large earthquakes, resulting from the recent progress in the field of image correlation of combined optical satellite images (Leprince et al. 2007; Rosu et al. 2015). We use high-resolution along-strike coseismic slip profiles of the 1992 M_w = 7.3 Landers, and 1999 M_w = 7.1 Hector Mine earthquakes from Milliner et al. (2016). Using subpixel correlation of satellite images, these authors produce profiles of right-lateral displacement every $\sim$ 140 m, over 60 km along the rupture profiles. Likewise, Vallage et al. (2015) combined optical satellite images to produce high-resolution 2-D maps of surface fault-parallel and fault-normal displacement due to the 2013 M_w 7.7 Balochistan earthquake in Pakistan. In this study, we consider the resulting profile of fault-parallel slip derived from far-field measurements ($>$1 km away from the scarp, as defined in Vallage et al. (2015)), sampled every 100 m for a 200 km-long rupture. Finally, we use the fault-parallel slip distribution at every 100 m produced by Klinger et al. (2018) for the 2016 M_w 7.8 Kaikoura earthquake in New Zealand. When the earthquake involves ruptures on multiple segments, the shown slip distribution is the one following the main rupture path. In order to compare all profiles adequately in the following spectral analysis, we interpolate them to obtain one measurement every 150 m, i.e., around 6 points per km. Figure 11 displays the coseismic fault-parallel displacement

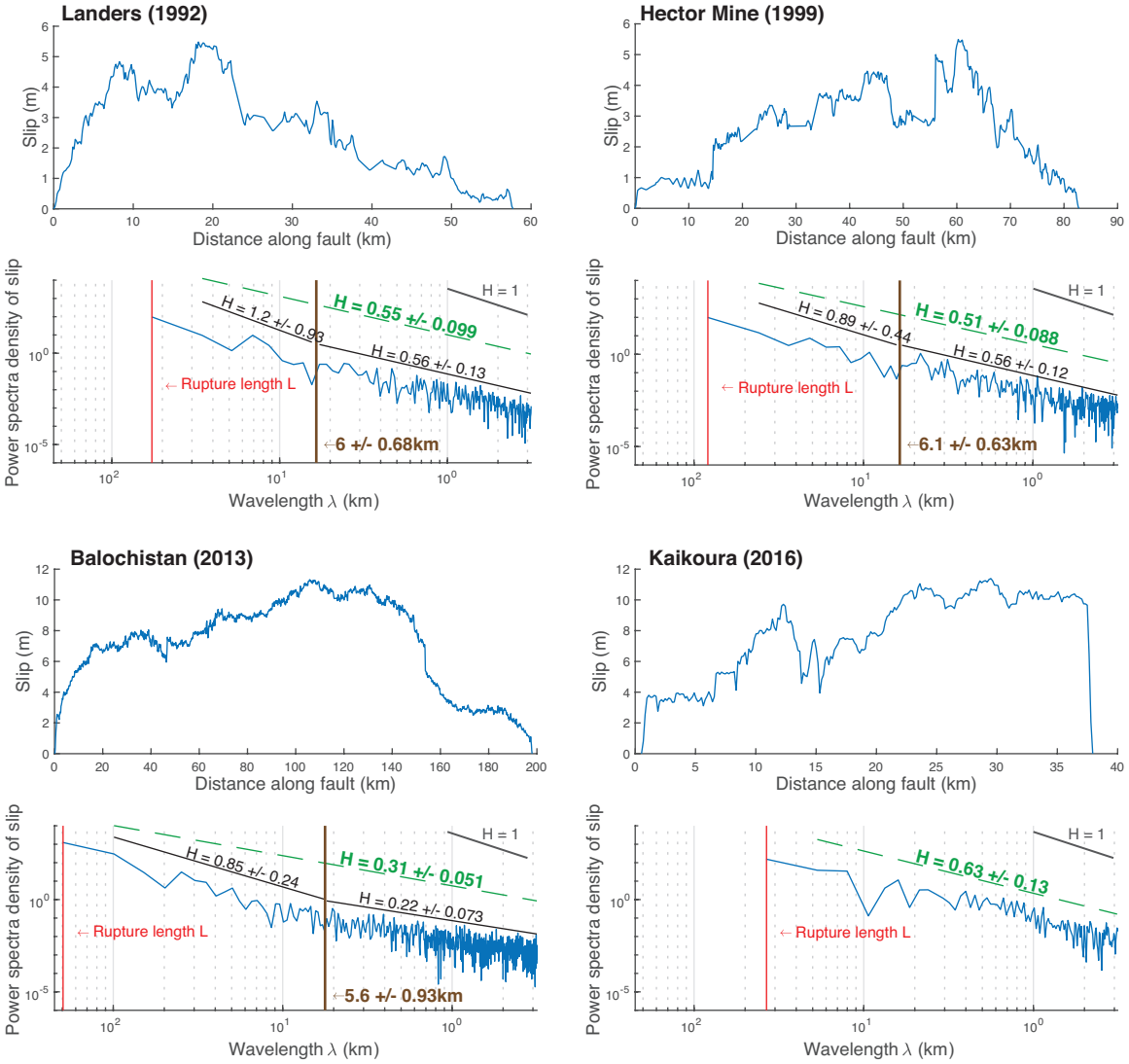

Figure 11. Coseismic slip profiles and associated power spectral densities of four large strike-slip earthquakes: the 1992 M_w = 7.3 Landers, the 1999 M_w = 7.1 Hector Mine, the 2013 M_w 7.7 Balochistan, and the 2016 M_w 7.8 Kaikoura events (Milliner et al. 2016; Vallage et al. 2015; Klinger et al. 2018). Hurst coefficients H are computed for all events. When the behavior at short wavelengths seems to vary, we estimate the critical wavelength at which the change occurs and then separately calculate Hurst coefficients for smaller and larger wavelengths.

distribution used in this study. For reference, we will also make use of the slip profile produced by the 2001 M_w7.8 Kunlun earthquake, displayed in Figure A2 (Klinger 2005). Note that compared to the other profiles, the resolution of this slip profile is inferior (up to one measurement per km).

Using the coseismic slip distributions, we follow the same procedure we developed with the numerically-generated slip profiles. We compute the power spectral density of each distribution, then derive the Hurst coefficient for wavelengths between the rupture length and the minimum wavelength

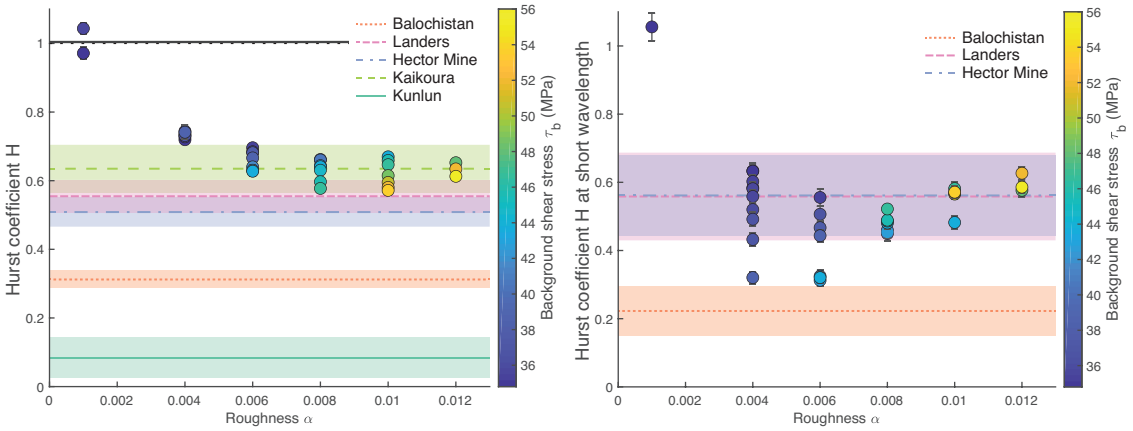

Figure 12. Comparison between the statistical analysis of mean Hurst coefficients from the numerically simulated slip profiles (as in Figures 2 and 7) with inferred Hurst coefficients from observed coseismic distributions.

considered here, i.e. 150 m. Resulting power spectral density are presented in Figure 11. Obtained Hurst coefficients range from 0.31 to 0.63, indicating that the final slip distributions are all self-affine, far from self-similarity. Once again, there appears to be a decrease in slope at shorter wavelengths. For instance the power spectral density for the Balochistan earthquake appears to flatten at wavelengths shorter than 5 km.

We estimate the location of this critical wavelength using the following procedure. For a given wavelength, we compute the slopes of the spectrum at smaller and larger wavelengths. This procedure is then repeated for all the wavelength range considered. We obtain curves of the evolution of the slope of the low and short wavelength ends (examples are displayed in Figure A3). A kink, or change in slope, will then appear as the minimum of the difference between these two slopes. For the Landers, Hector Mine, and Balochistan events, this kink seems to be located around 6 km. The procedure could not find a kink in the power spectral density for the Kaikoura earthquake. For both the Landers and Hector Mine earthquakes, the Hurst coefficients at shorter wavelengths have similar values, around 0.56, compared to the ones computed over the entire wavelength domain. On the other side, the power spectral density of the Balochistan event shows a lower value of Hurst coefficient at shorter wavelengths, indicating a greater amplitude at short wavelengths.

We now compare our results from the numerical simulations, obtained in the previous section, with values of Hurst coefficients that we computed from real coseismic displacement profiles. Figure 12 illustrates the distribution of the mean Hurst coefficient of numerically-generated slip profiles over the entire wavelength domain and at very short wavelengths ($\lambda < 1$ km) as presented in Figures 3 and 7. We superimpose the computed values of Hurst coefficients from all considered earthquakes. Due to the lack of short wavelengths, or to a different behavior at short wavelengths, we only plot

results from the Landers, Hector Mine, and Balochistan earthquakes on the figure that displays Hurst coefficients computed at short wavelengths. We first notice that while the range of Hurst coefficients of the slip distributions covered by the numerical simulations range from 1 to 0.55, the Hurst coefficients inferred from the coseismic slip profiles all lie below 0.65. The slip distributions from the Landers, Hector Mine, and Kaikoura earthquakes present Hurst coefficients around 0.5-0.6, close to range of the numerical simulations, but still difficult to distinguish due to the high uncertainty. On the other hand, Hurst coefficients computed from the slip profiles of the Balochistan and Kunlun earthquakes range between 0 and 0.3, setting them away from the levels observed in numerical simulations. When comparing the slope of slip spectra at short wavelengths, there is a similar agreement between numerical simulations and observed slip distributions. The Hurst coefficients obtained for the Landers and Hector Mine earthquakes lie within the same range as the numerical simulations; however, the large uncertainties prevent from drawing any conclusions about the fault roughness. The Balochistan event again has short wavelength amplitudes that are higher than any simulations.

5 DISCUSSION

In this study, we investigated the characteristics of slip distributions generated on rough faults. The overarching goal of this approach is to evaluate if we can deduce information about fault roughness and rupture processes in observed coseismic displacement profiles. We first documented the spectral characteristics of slip distributions with respect of roughness and background shear stress. We showed that even though all profiles were generated on self-similar profiles, the slip profiles become increasingly more self-affine with higher fault roughness α (Figure 3). There is no obvious agreement between the fractal dimension of the fault profile and the one of the resulting slip distribution. This is unexpected, because slip perturbations are expected to have the same statistical properties than the local geometry, as shown by Dunham et al. (2011b), at least a the first-order static perturbation analysis. Differences might be due to rupture processes and dynamic effects which, together with fault geometry, either create more short wavelength slip fluctuations or suppress long wavelength slip, leading to a self-affine distribution. When separating sub-Rayleigh from supershear ruptures, we noticed that the deviation from self-similarity grows linearly with fault roughness. Slip distributions from supershear ruptures are systematically self-affine, with Hurst coefficients around 0.6 (Figure 4). We finally showed that the amplitude of the slip profile increases linearly with the background shear stress. The fault roughness does not seem to have such an effect that is not already captured by the need for higher background shear stress to initially rupture (Figure 9).

Results from numerical simulations revealed that roughness and background shear stress affect the fractal dimension of the produced slip distribution. This control might, however, be affected by

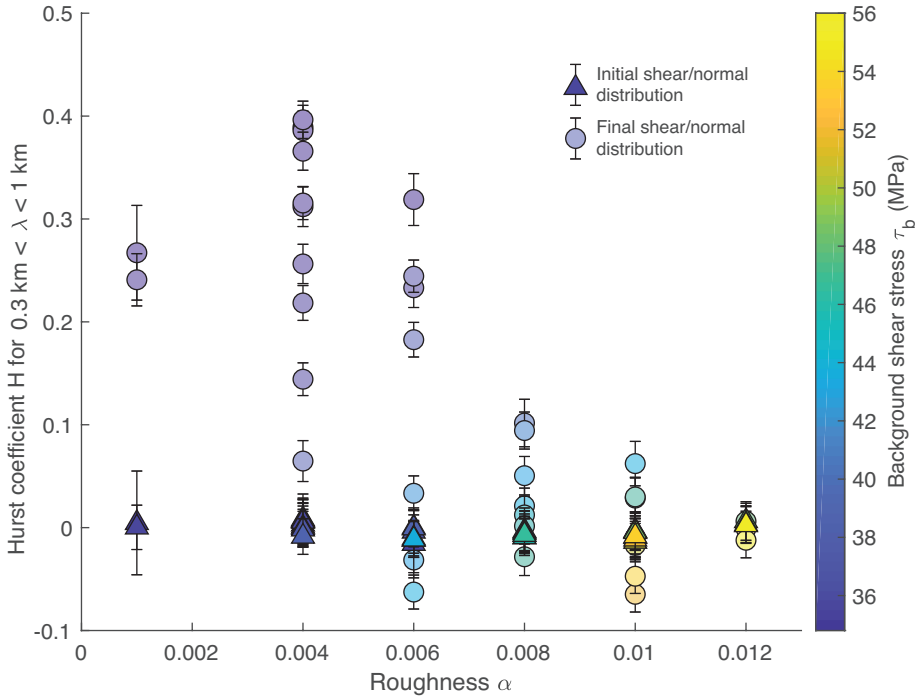

Figure 13. Distribution of the Hurst coefficient of the power spectral densities of the initial (triangles) and final (circles) shear-to-normal distribution at very short wavelengths (λ <1 km) as a function of roughness and background shear stress.

the set of parameters we chose to characterize the elasto-viscoplastic rheology of the off-fault material. We test this idea by running additional simulations for different values of plastic dilatancy β and Drucker-Prager viscosity η in the medium surrounding the fault (see details about the tested parameters in Appendix A). Figure A1 shows that there are only slight changes between the Hurst coefficients obtained for the original simulations and the ones obtained with different off-fault characteristics. These slight changes are not capable of explaining the large variation in Hurst coefficients with roughness and background shear stress we observed in the earliest sections. Thus, the deviations from self-similarity that can be observed in slip distributions do not seem to be related to the material properties of the surrounding material.

When looking at individual sets of power spectral densities, we realized that the slope, at which the density decreases, also varies with the wavelength range. We showed that there seemed to be a critical wavelength (around 1 km in our simulations) above which the power at short wavelengths varies with roughness and background shear stress (Figures 5 and 6). Slip profiles from sub-Rayleigh ruptures show clearly greater power in short wavelengths (i.e., lower Hurst coefficient) with increasing roughness and background shear stress. Differently, the Hurst coefficient of supershear slip profiles increases with roughness (Figure 8). For such a simple 2D numerical set-up, the existence of a crit-

ical wavelength is puzzling. As it appears clearly in the power spectral density of the slip gradient (Figure 6), we first investigate whether the initial shear-to-normal stress distribution can explain the slip variability. We perform the same spectral analysis for the initial and final shear-to-normal stress distribution, and compute the Hurst coefficient at short wavelengths. Figure 13 presents the Hurst coefficient evolution with roughness and background shear stress, while the power spectral densities are given in Figures A4 and A5. The initial shear-to-normal distributions all have Hurst coefficient around zero. Neither the roughness nor the background shear stress seem to affect the Hurst coefficients. Note that this does not apply for the final shear-to-normal distributions whose Hurst coefficients greatly differ from the ones of the initial distributions and vary with roughness and background shear stress. We anticipate that over multiple earthquake cycles, the characteristics of the shear-to-normal distribution might change between subsequent events. The statistical characteristics of the slip distribution after multiple ruptures on a single fault might vary from the slip pattern of the single ruptures we are investigating in this study. While beyond the scope of this work, this issue merits further study.

To explain the presence of a critical length scale, we also investigate whether there is any correlation between slip gradient, the slope $m(x) = \partial h/\partial x$, and rupture velocity. Unfortunately, correlations displayed Figure A6 show that no correlations appear between the slip gradient and the fault slope. Only the correlation between slope and rupture velocity, already observed in Fang & Dunham (2013), emerges here. Finally, given that the ruptures are all self-healing slip pulses, the length of the pulse might play a role in this critical length scale. Differences in the Hurst coefficient for sub-Rayleigh vs. supershear ruptures suggest a control from the process zone, and subsequently the pulse width. Coincidentally, from the examples given in Bruhat et al. (2016), the pulse width seems to be also around 1 km. Further work is required on the numerical side to confirm the existence of this critical wavelength, estimate it origin, and determine whether it is fully controlled by the fault roughness or other properties of the rupture.

When comparing with measured coseismic slip, the Hurst coefficients obtained from numerical simulations most often overestimate the ones observed in real slip distributions. Only the Landers and Hector Mine ruptures present Hurst coefficients in the same range as the simulations. However, the large uncertainties and the complexity revealed in the earlier analysis of the numerical simulations make it difficult, for now, to relate the spectral signature of real earthquakes to fault roughness. Explanations for this negative result are multiple. First, we use a simplified fault model that does not consider other possible controls on slip heterogeneity, such as previous slip history, afterslip, poroelastic effects (Hirakawa & Ma 2018), and most importantly, re-roughening mechanisms, such as segmentation or branching. Although the first processes would likely smooth out short wavelength features since they are associated with relaxation of stress concentrations, re-roughening mechanisms, which

play an important role in fault evolution, are plausible causes for slip profiles with low Hurst coefficients. Moreover, while we set aside the Kunlun earthquake because of the lack of short wavelengths, the corresponding slip distribution has a very different spectral content, with Hurst coefficient close to zero (Figure A2). Unlike the other earthquakes, this event ruptured permafrost (Klinger 2005), which acts brittle and offers little chance for damping or distributed deformation in the surrounding environment. This could result in a slip distribution with higher short wavelength content. Finally, our model ignores 3D effects, which might affect the resulting slip distribution at the surface. Although dynamic ruptures on rough fault surfaces in 3D are currently developed (Duru & Dunham 2016; Yao 2017; Williams et al. 2018), the computational cost is still too high to produce ruptures catalogs for use in statistical analysis of rupture complexity.

An obvious explanation of the observed discrepancy between numerical modeling and recorded coseismic slip might originate from the assumption of self-similarity of the fault geometry. All the synthetic fault traces were generated as self-similar faults. Self-similar faults are commonly used in numerical simulations since they have the power to connect roughness measurements across all scales, from the outcrop to the map. The trade-off in Hurst coefficients observed in this study raises questions about using self-similar faults in the first place. This issue arises also when distinguishing sub-Rayleigh from supershear ruptures. As supershear ruptures are often considered to occur on fault segments that are smoother at long wavelengths (Bouchon et al. 2010), this would a priori suggest using a self-affine fault profile. Meanwhile, numerical studies, such as Bruhat et al. (2016), showed that self-similar fault profiles are likewise useful to study characteristics of supershear ruptures on rough faults. This could also mean that, while one often focuses on the Hurst coefficient for estimating the fault nonplanarity, the main factor that controls the rupture behavior would be in fact the amplitude-to-wavelength ratio α. Future work might either consider self-affine faults as a starting point, exploring whether it would affect rupture and slip behavior, or investigate the role of the Hurst coefficient with respect to the amplitude-to-wavelength ratio α.

A notable difference between the synthetic and observed slip distributions is the presence of a critical wavelength under which the power spectral density flattens. While this critical wavelength always occurred at $\lambda < 1$ km in the numerical simulations, it occurs around 5-6 km for the Landers, Hector Mine, and Balochistan events. On the other hand, it remains difficult to see any change in slope in the power spectral density for the Kaikoura earthquake. Taken at face value, we cannot make any connection between the critical wavelength noticed in synthetic slip profiles and the one inferred for the Landers, Hector Mine, and Balochistan earthquakes. The latter might inform us about a segmentation or seismogenic length, as suggested in Klinger (2010). It could also simply reveal a critical asperity size that would resist abrasional wear and fracturing. This hypothesis was already mentioned

in Milliner et al. (2015) when analyzing the Landers earthquake, where the authors actually predicted a "a second roll-off or 'whitening at higher wave numbers". Unfortunately, the authors did not seem to detect the critical wavelength we found in this study, possibly due to the fact that they were analyzing only one rupture.

Our study started with the idea that geometrical complexity such as fault roughness possibly leaves an imprint in the produced slip distribution, and that if this signature is somewhat quantifiable, we would be able to infer properties of fault roughness from past slip distributions. Using dynamic modeling of earthquakes on rough faults, we showed that the connection between fault roughness and the spectral content of the slip distribution is much more complex, as it might depend on the initial fault geometry and the rupture behavior. While rupture behavior and dynamic effects might explain the complexity seen in numerical modeling, geometric complexities, like branches or segmentation, and wear processes might play an additional role in the real Earth. We hope, however, that the current development of high-resolution measurements of coseismic slip distribution will help us uncover the relationship between fault roughness and surface displacement.

ACKNOWLEDGMENTS

This work was supported by the ANR Geosmec ANR-12-BS06-0016. Simulations were done using the finite difference code FDMAP. Code and input files are available at https://bitbucket.org/ericmdunham/fdmap. We thank Jérôme Aubry, Alexandre Schubnel, Harsha S. Bhat, and Ahmed Elbanna for stimulating discussions. We also thank the Associate Editor Eiichi Fukuyama, Michel Bouchon, and an anonymous reviewer for their encouraging and insightful comments.

REFERENCES

Andrews, D. J., 1980. A stochastic fault model: 1. Static case, *Journal of Geophysical Research*, **85**(B7), 3867.

Bilby, B. A. & Eshelby, J. D., 1968. Dislocations and the theory of fracture, in *Fracture, an advanced treatise*, pp. 99–182, Academic Press New York and London.

Bouchon, M., Karabulut, H., Bouin, M. P., Schmittbuhl, J., Vallée, M., Archuleta, R., Das, S., Renard, F., & Marsan, D., 2010. Faulting characteristics of supershear earthquakes, *Tectonophysics*, **493**(3-4), 244–253.

Brodsky, E. E., Gilchrist, J. J., Sagy, A., & Collettini, C., 2011. Faults smooth gradually as a function of slip, *Earth and Planetary Science Letters*, **302**(1-2), 185–193.

Bruhat, L., Fang, Z., & Dunham, E. M., 2016. Rupture complexity and the supershear transition on rough faults, *Journal of Geophysical Research: Solid Earth*, **121**(1), 210–224.

Bürgmann, R., Pollard, D. D., & Martel, S. J., 1994. Slip distributions on faults: effects of stress gradients,

inelastic deformation, heterogeneous host-rock stiffness, and fault interaction, *Journal of Structural Geology*, **16**(12), 1675–1690.

Candela, T., Renard, F., Bouchon, M., Brouste, A., Marsan, D., Schmittbuhl, J., & Voisin, C., 2009. Characterization of fault roughness at various scales: Implications of three-dimensional high resolution topography measurements, *Pure and Applied Geophysics*, **166**(10-11), 1817–1851.

Candela, T., Renard, F., Klinger, Y., Mair, K., Schmittbuhl, J., & Brodsky, E. E., 2012. Roughness of fault surfaces over nine decades of length scales, *Journal of Geophysical Research: Solid Earth*, **117**(B8).

Chester, F. M. & Chester, J. S., 2000. Stress and deformation along wavy frictional faults, *Journal of Geophysical Research*, **105**(B10), 23421–23430.

Choi, J.-H., Klinger, Y., Ferry, M., Ritz, J.-F., Kurtz, R., Rizza, M., Bollinger, L., Davaasambuu, B., Tsend-Ayush, N., & Demberel, S., 2018. Geologic Inheritance and Earthquake Rupture Processes: The 1905 M 8 Tsetserleg-Bulnay Strike-Slip Earthquake Sequence, Mongolia, *Journal of Geophysical Research: Solid Earth*, **123**(2), 1925–1953.

Dieterich, J. H. & Smith, D. E., 2009. Nonplanar Faults: Mechanics of Slip and Off-fault Damage, *Pure and Applied Geophysics*, **166**(10-11), 1799–1815.

Dunham, E. M., Belanger, D., Cong, L., & Kozdon, J. E., 2011a. Earthquake Ruptures with Strongly Rate-Weakening Friction and Off-Fault Plasticity, Part 1: Planar Faults, *Bulletin of the Seismological Society of America*, **101**(5), 2296–2307.

Dunham, E. M., Belanger, D., Cong, L., & Kozdon, J. E., 2011b. Earthquake ruptures with strongly rate-weakening friction and off-fault plasticity, Part 2: Nonplanar faults, *Bulletin of the Seismological Society of America*, **101**(5), 2308–2322.

Duru, K. & Dunham, E. M., 2016. Dynamic earthquake rupture simulations on nonplanar faults embedded in 3D geometrically complex, heterogeneous elastic solids, *Journal of Computational Physics*, **305**, 185–207.

Fang, Z. & Dunham, E. M., 2013. Additional shear resistance from fault roughness and stress levels on geometrically complex faults, *Journal of Geophysical Research: Solid Earth*, **118**(7), 3642–3654.

Harbord, C. W., Nielsen, S. B., De Paola, N., & Holdsworth, R. E., 2017. Earthquake nucleation on rough faults, *Geology*, **45**(10), 931–934.

Haskell, N., 1964. Total energy and energy spectral density of elastic wave radiation from propagating faults, *Bulletin of the Seismological Society of America*, **54**(6), 1811–1841.

Hirakawa, E. & Ma, S., 2018. Undrained Gouge Plasticity Stabilizes Rupture Dynamics of Rough Faults, *Bulletin of the Seismological Society of America*.

Huang, Y. & Gao, H., 2001. Intersonic Crack PropagationPart I: The Fundamental Solution, *Journal of Applied Mechanics*, **68**(2), 169.

Klinger, Y., 2005. High-Resolution Satellite Imagery Mapping of the Surface Rupture and Slip Distribution of the Mw 7.8, 14 November 2001 Kokoxili Earthquake, Kunlun Fault, Northern Tibet, China, *Bulletin of the Seismological Society of America*, **95**(5), 1970–1987.

Klinger, Y., 2010. Relation between continental strike-slip earthquake segmentation and thickness of the crust,

Journal of Geophysical Research, **115**(B7), B07306.

Klinger, Y., Etchebes, M., Tapponnier, P., & Narteau, C., 2011. Characteristic slip for five great earthquakes along the Fuyun fault in China, *Nature Geoscience*, **4**(6), 389–392.

Klinger, Y., Okubo, K., Vallage, A., Champenois, J., Delorme, A., Rougier, E., Lei, Z., Knight, E. E., Munjiza, A., Satriano, C., Baize, S., Langridge, R., & Bhat, H. S., 2018. Earthquake damage patterns resolve complex rupture processes, *Geophysical Research Letters*.

Kozdon, J. E., Dunham, E. M., & Nordström, J., 2012. Interaction of Waves with Frictional Interfaces Using Summation-by-Parts Difference Operators: Weak Enforcement of Nonlinear Boundary Conditions, *Journal of Scientific Computing*, **50**(2), 341–367.

Kozdon, J. E., Dunham, E. M., & Nordström, J., 2013. Simulation of dynamic earthquake ruptures in complex geometries using high-order finite difference methods, *Journal of Scientific Computing*, **55**(1), 92–124.

Leprince, S., Barbot, S., Ayoub, F., & Avouac, J.-P., 2007. Automatic and Precise Orthorectification, Coregistration, and Subpixel Correlation of Satellite Images, Application to Ground Deformation Measurements, *IEEE Transactions on Geoscience and Remote Sensing*, **45**(6), 1529–1558.

Manighetti, I., Campillo, M., Sammis, C., Mai, P., & King, G., 2005. Evidence for self-similar, triangular slip distributions on earthquakes: Implications for earthquake and fault mechanics, *Journal of Geophysical Research*, **110**(B5), B05302.

Milliner, C. W. D., Dolan, J. F., Hollingsworth, J., Leprince, S., Ayoub, F., & Sammis, C. G., 2015. Quantifying near-field and off-fault deformation patterns of the 1992 M w 7.3 Landers earthquake, *Geochemistry, Geophysics, Geosystems*, **16**(5), 1577–1598.

Milliner, C. W. D., Sammis, C., Allam, A. A., Dolan, J. F., Hollingsworth, J., Leprince, S., & Ayoub, F., 2016. Resolving Fine-Scale Heterogeneity of Co-seismic Slip and the Relation to Fault Structure, *Scientific Reports*, **6**(1), 27201.

Ozawa, S. W., Hatano, T., & Kame, N., 2019. Longer Migration and Spontaneous Decay of Aseismic Slip Pulse Caused by Fault Roughness, *Geophysical Research Letters*, **46**(2), 636–643.

Power, W. L. & Tullis, T. E., 1991. Euclidean and fractal models for the description of rock surface roughness, *Journal of Geophysical Research*, **96**(B1), 415–424.

Power, W. L. & Tullis, T. E., 1995. A review of the fractal character of natural fault surfaces with implications for friction and the evolution of fault zones, in *Fractals in the Earth Sciences*, pp. 89–105, Springer.

Renard, F., Voisin, C., Marsan, D., & Schmittbuhl, J., 2006. High resolution 3D laser scanner measurements of a strike-slip fault quantify its morphological anisotropy at all scales, *Geophysical Research Letters*, **33**(4), L04305.

Rosu, A.-M., Pierrot-Deseilligny, M., Delorme, A., Binet, R., & Klinger, Y., 2015. Measurement of ground displacement from optical satellite image correlation using the free open-source software MicMac, *ISPRS Journal of Photogrammetry and Remote Sensing*, **100**, 48–59.

Sagy, A. & Brodsky, E. E., 2009. Geometric and rheological asperities in an exposed fault zone, *Journal of Geophysical Research*, **114**(B2).

Sagy, A., Brodsky, E. E., & Axen, G. J., 2007. Evolution of fault-surface roughness with slip, *Geology*, **35**(3), 283.

Scholz, C. H., 2019. Mechanics of faulting, in *The Mechanics of Earthquakes and Faulting*, pp. 97–165, Cambridge University Press.

Shervais, K. A. & Kirkpatrick, J. D., 2016. Smoothing and re-roughening processes: The geometric evolution of a single fault zone, *Journal of Structural Geology*, **91**, 130–143.

Shi, Z. & Day, S. M., 2013. Rupture dynamics and ground motion from 3-D rough-fault simulations, *Journal of Geophysical Research: Solid Earth*, **118**(3), 1122–1141.

Spudich, P. & Frazer, L., 1984. Use of ray theory to calculate high-frequency radiation from earthquake sources having spatially variable rupture velocity and stress drop, *Bulletin of the Seismological Society of America*, **74**(6), 2061–2082.

Tal, Y. & Hager, B. H., 2018. The Slip Behavior and Source Parameters for Spontaneous Slip Events on Rough Faults Subjected to Slow Tectonic Loading, *Journal of Geophysical Research: Solid Earth*, **123**(2), 1810–1823.

Tal, Y., Hager, B. H., & Ampuero, J. P., 2018. The Effects of Fault Roughness on the Earthquake Nucleation Process, *Journal of Geophysical Research: Solid Earth*, **123**(1), 437–456.

Turcotte, D. L. & Huang, J., 1995. Fractal Distributions in Geology, Scale Invariance, and Deterministic Chaos, in *Fractals in the Earth Sciences*, pp. 1–40, eds Barton, C. C. & La Pointe, P. R., Springer US, Boston, MA.

Ulrich, T., Gabriel, A.-A., Ampuero, J.-P., & Xu, W., 2019. Dynamic viability of the 2016 Mw 7.8 Kaikura earthquake cascade on weak crustal faults, *Nature Communications*, **10**(1), 1213.

Vallage, A., Klinger, Y., Grandin, R., Bhat, H. S., & Pierrot-Deseilligny, M., 2015. Inelastic surface deformation during the 2013 M w 7.7 Balochistan, Pakistan, earthquake, *Geology*, p. G37290.1.

Williams, M. C. B., Duru, K., Gabriel, A. A., & Dunham, E. M., 2018. 3D Dynamic Rupture on Fractally Rough Faults in Random Heterogeneous Media, *Abstract S43A-01 presented at 2018 Fall Meeting, AGU, Washington DC, 1014 Dec.*.

Yao, Q., 2017. *Dynamic Modeling of Earthquake Sources on Rough Faults*, Ph.D. thesis, University of California, San Diego.

Zheng, G. & Rice, J. R., 1998. Conditions under which velocity-weakening friction allows a self-healing versus a cracklike mode of rupture, *Bulletin of the Seismological Society of America*, **88**(6), 1466–1483.

Zielke, O., Galis, M., & Mai, P. M., 2017. Fault roughness and strength heterogeneity control earthquake size and stress drop, *Geophysical Research Letters*, **44**(2), 777–783.

APPENDIX A: INFLUENCE OF OFF-FAULT MATERIAL PARAMETERS

We test here whether changes in the degree of plastic dilatancy β and Drucker-Prager viscosity η in the medium surrounding the fault affect slip profiles computed from numerical simulations. The plastic dilatancy β is defined as the ratio of volumetric to shear plastic strain. To be consistent with laboratory experiments measuring dilatancy, Dunham et al. (2011a,b) chose β as

$$\beta = \frac{\mu}{2}, \tag{A.1}$$

where μ the Drucker-Prager internal friction parameter.

The Drucker-Prager viscosity η is chosen here as

$$\eta = 0.1 G t_c \tag{A.2}$$

with G shear modulus and t_c the characteristic time t_c in the simulations, controlled by the S-wave speed c_S and process zone length R_0, such that $t_c = R_0/c_S$. A nonzero η is used in the viscoplastic rheology to ensure well-posed numerical simulations that converge with mesh refinement. The model, as defined, has two characteristic timescales: the viscoplastic relaxation time, η/G, and the characteristic wave transit time across the state-evolution region, R_0/c_s. The latter also characterizes the timescale over which frictional weakening occurs at the rupture front. A dimensionless ratio of those two terms is thus given by

$$\xi = (\eta/G)/(R_0/c_s). \tag{A.3}$$

When $\xi \ll 1$, then plasticity is important even during the rapid weakening process at the rupture front. Otherwise, the material response around the rupture front is effectively elastic. In the reference catalog $\xi = 0.1$.

Figure A1 presents the evolution of the Hurst coefficients at short wavelengths ($\lambda < 1\ km$) as a function of background shear stress. The original simulations, used in Fang & Dunham (2013) and Bruhat et al. (2016), are indicated in black. Colored error bars correspond to the new set of simulations with different material parameters. We test simulations with a lower β (half the original value) and β = 0 (no dilatancy). Additionally, we test values of ξ to half and to twice of its original value. Most simulations are run for $\alpha = 0.006$, but we also make some tests at different roughness levels. There seems to be no dramatic change between the simulations, especially in order to reach the range covered by the data displayed in Figure 12.

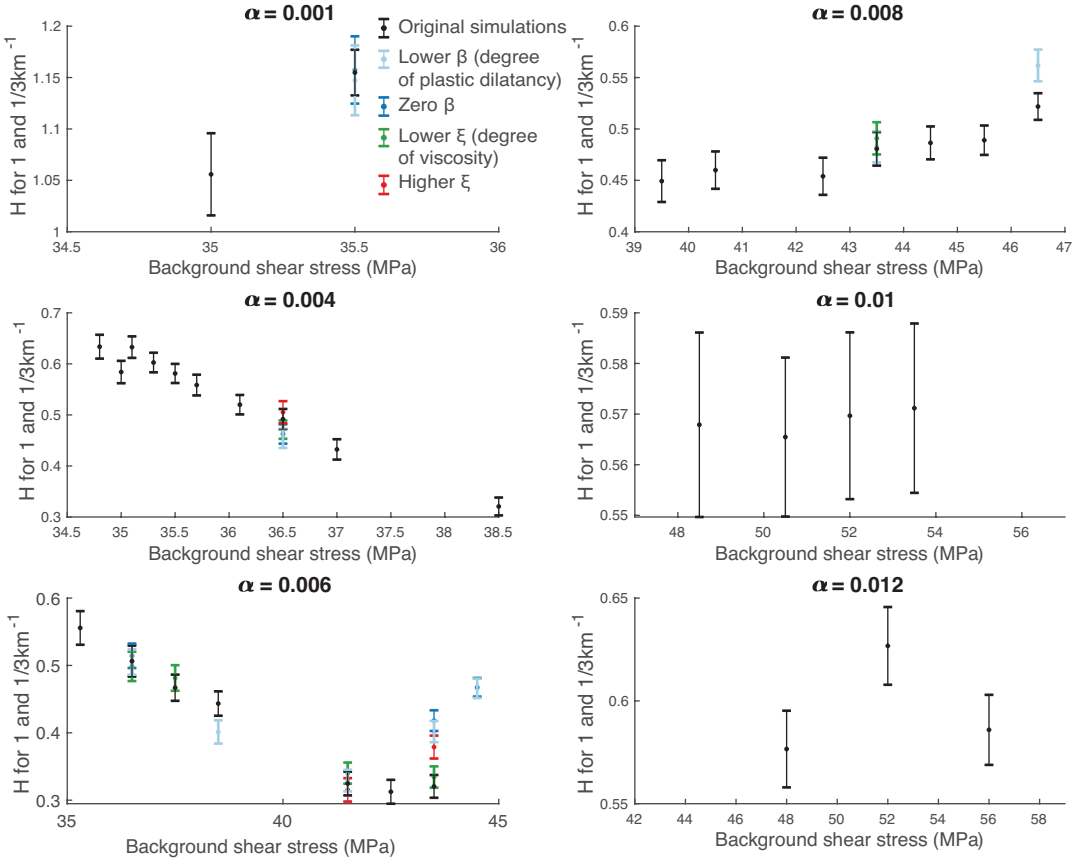

Figure A1. Evolution of Hurst coefficients at short wavelengths ($\lambda < 1$) as a function of background shear stress. Error bars are for 1-σ uncertainties. Black error bars are for simulations with the same parameters for off-fault materials used in Fang & Dunham (2013) and Bruhat et al. (2016). Colored errors bars correspond to plastic dilatancy or viscosity changes.

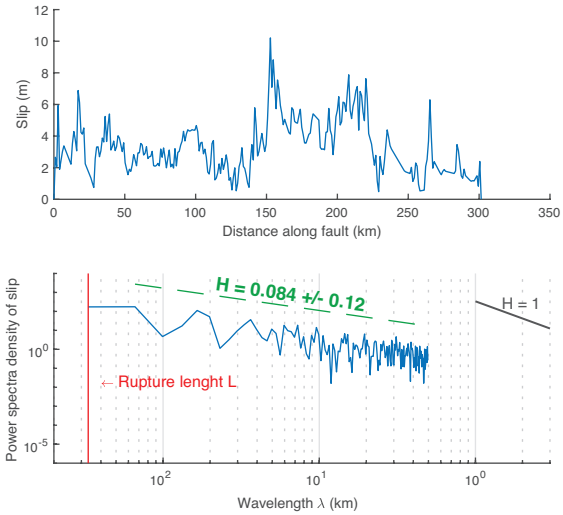

Figure A2. Top) Coseismic slip profile of the 2001 M_w7.8 Kunlun earthquake from Klinger (2005). (Bottom) Power spectral density of the slip profile and corresponding Hurst coefficient. Due to a sparser sampling (up to one measurement per km), the slip spectrum is limited to wavelengths greater than 2 km.

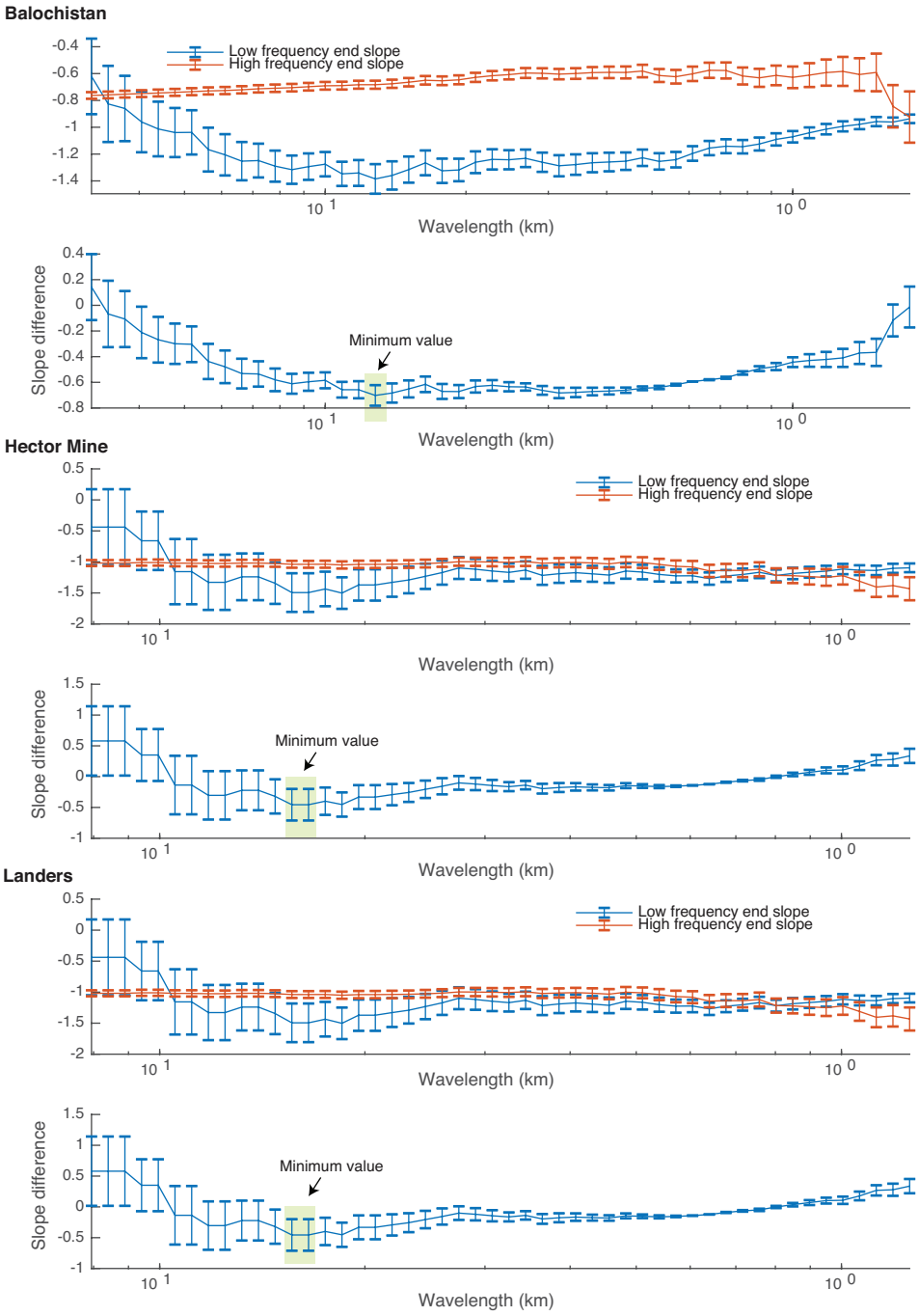

Figure A3. Procedure to estimate the wavelength at which a kink occurs in the slip spectrum. For each wavelength, the slope of the spectrum on its right (at higher frequency) and left (at lower frequency) sides are computed. If there is a kink in the slip spectrum, it will appear at the minimum value of the difference between these two slopes.

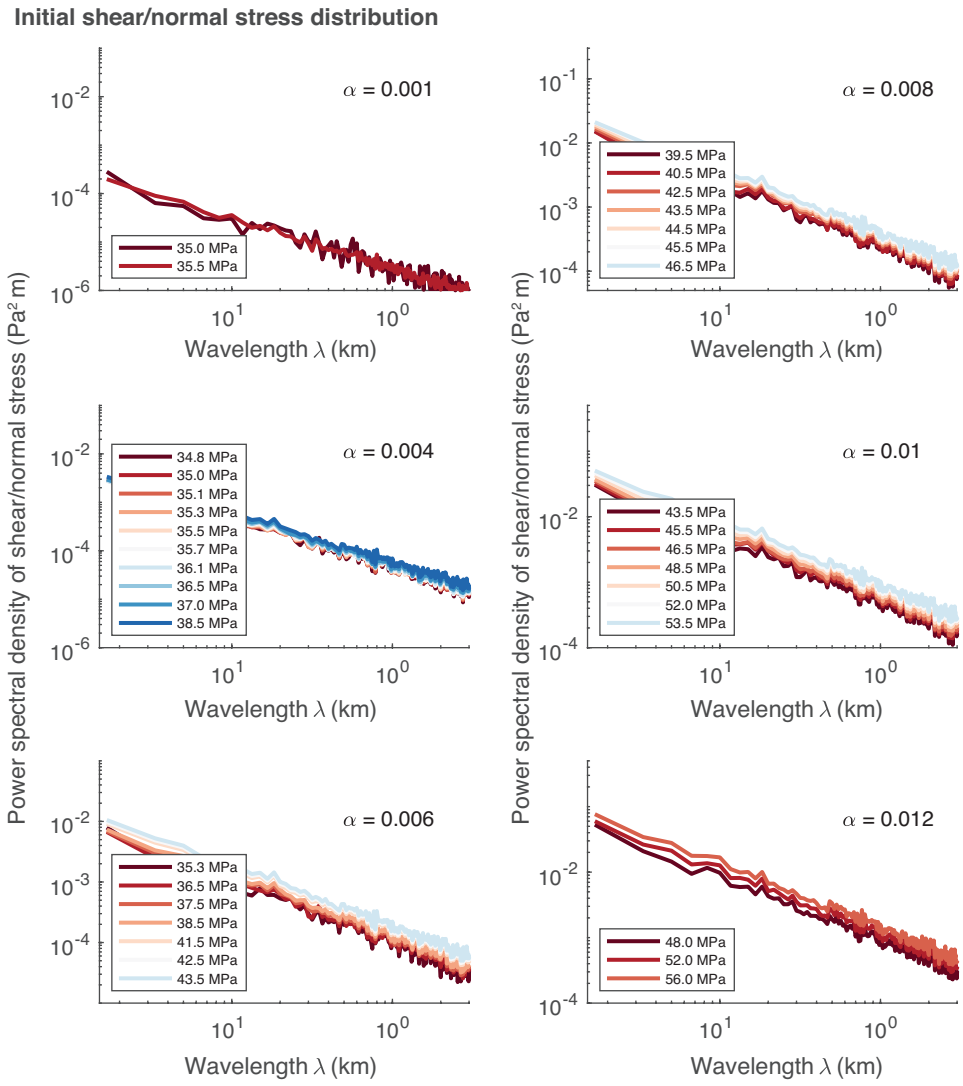

Figure A4. Mean power spectral density of initial shear-to-normal stress distributions as a function of the wavelength λ and background shear stress, for roughness values from $\alpha = 0.001$ to 0.012.

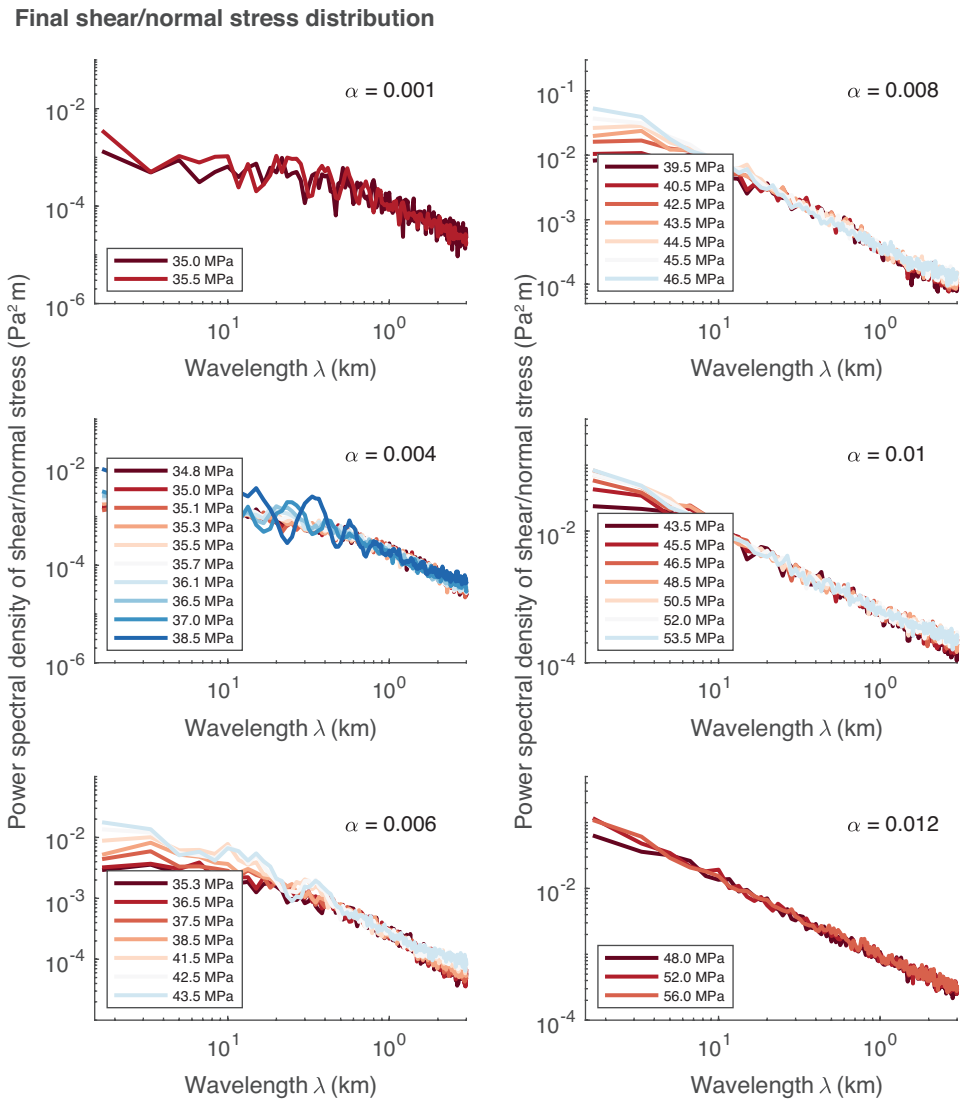

Figure A5. Mean power spectral density of final shear-to-normal stress distributions as a function of the wavelength λ and background shear stress, for roughness values from $\alpha = 0.001$ to 0.012.

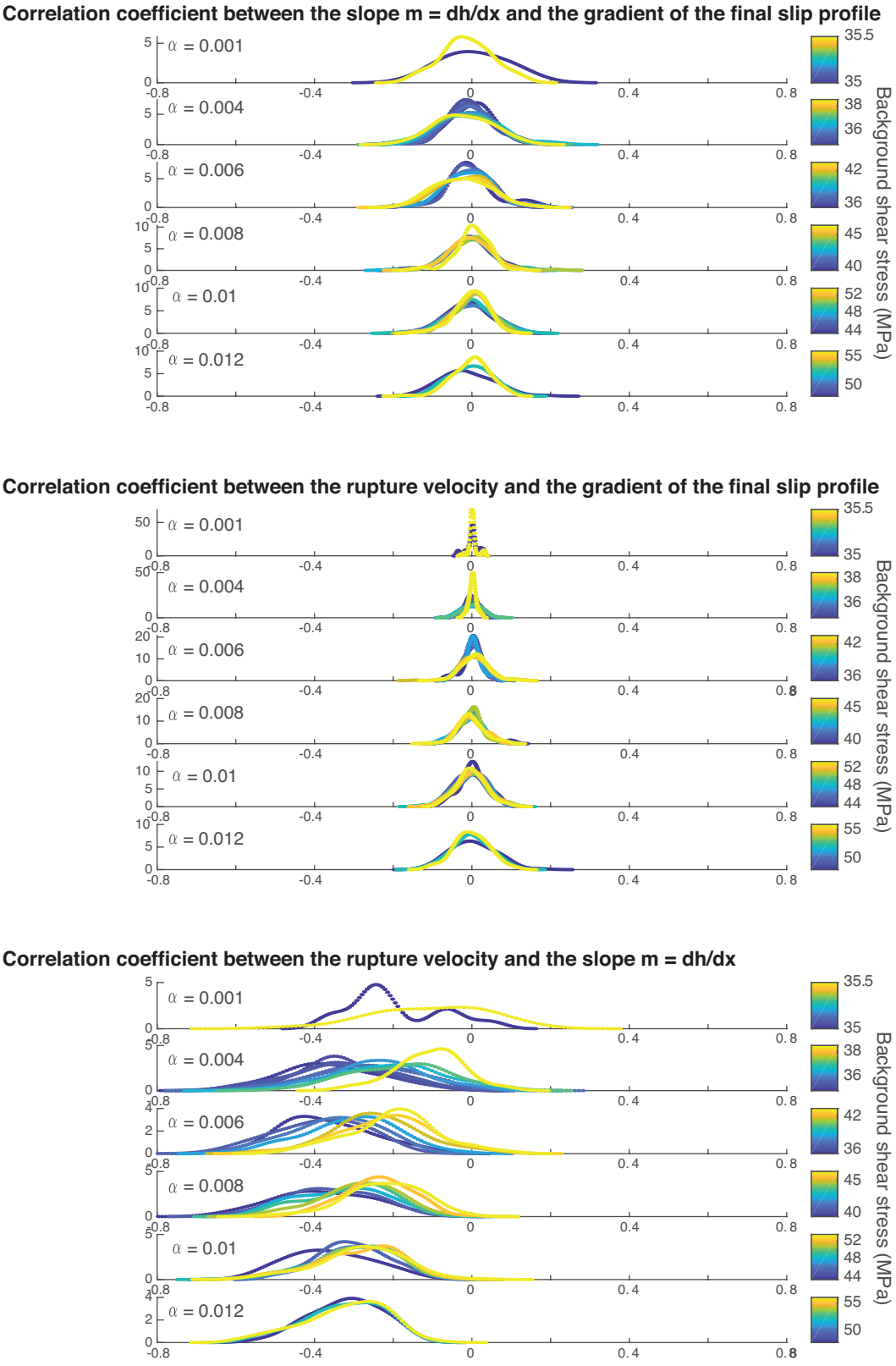

Figure A6. Correlation coefficients between the fault slope $m(x) = \partial y/\partial x$, the gradient of the final slip distribution and the rupture velocity, for all considered roughness α and background shear stress. We only observe the negative correlation between slope and rupture velocity that was already noticed in Fang & Dunham (2013).